

Contents lists available at ScienceDirect

Lithos

journal homepage: www.elsevier.com/locate/lithos



Research Article

Post-collisional volcanism with adakitic signatures in the Arabian-Nubian Shield: A case study of calc-alkaline Dokhan volcanics in the Eastern Desert of Egypt



Bassam A. Abuamarah ^{a,*}, Mokhles K. Azer ^b, Paul D. Asimow ^c, Qingshang Shi ^d

- ^a Department of Geology and Geophysics, King Saud University, Riyadh 11451, Saudi Arabia
- ^b Geological Sciences Department, National Research Centre, 12622-Dokki, Cairo, Egypt
- ^c Division of Geological & Planetary Sciences, California Institute of Technology, Pasadena, CA 91125, USA
- d State Key Laboratory of Geological Processes and Mineral Resources, School of Earth Science and Resources, China University of Geosciences, Beijing 100083, China

ARTICLE INFO

Article history: Received 21 December 2020 Received in revised form 9 February 2021 Accepted 11 February 2021 Available online 15 February 2021

Keywords: Arabian-Nubian Shield Post-collisional volcanics Lithospheric delamination Adakite Pyrophanite

ABSTRACT

A volcano-sedimentary succession, including the Guruf volcanic series, is exposed at Gabal Um Guruf in the north Eastern Desert of Egypt. A series of intermediate to silicic volcanic flows and associated pyroclastic deposits unconformably overlie quartz-diorite and granodiorite plutons and are intruded by high-level alkali feldspar granites. The metavolcanic xenoliths in the granodiorite are shown to be unrelated to the Guruf volcanics. Two volcanic cycles can be recognized. The lower unit is a high-K calc-alkaline series with minor basaltic andesite and mostly andesite through dacite. The upper unit consists of rhyolite and rhyodacite that is transitional towards alkaline, A-type magma. Both units are assigned to the Dokhan volcanics and interpreted as post-collisional. REE patterns are characterized by slow progressive enrichment throughout the suite, with heavy REE apparently acting more incompatibly than light REE; concave-upwards REE patterns in basalt andesite suggest residual amphibole in the source. Only the upper rhyolite displays prominent negative Eu anomalies (Eu/Eu * = 0.35–0.73). Apparent crystallization temperatures of primary pyroxene are 800-1000 °C and of primary amphiboles 781–944 °C. The major and trace element chemistry of the suite can be modeled as a single liquid line of descent, with pressure decreasing as the magma cools and evolves, and a prominent role for apatite in sequestering CaO, P₂O₅, and light REE. Although upper crustal contamination and magma mixing cannot be ruled out, the data do not require them. The suite includes pyrophanite, an unusual Mn-rich ilmenite-group solid solution, not previously recorded in volcanic rocks in the Arabian-Nubian Shield (ANS). The Guruf volcanic series is undeformed and unmetamorphosed, unlike the typical subduction-related volcanic units of the ANS. The geochemical characteristics are consistent with those of many post-collisional ANS rocks. The mostly calc-alkaline character and other traits previously interpreted to indicate an active arc setting instead more likely reflect remelting of earlier arc-related material from the pre-collisional stage (850–740 Ma). The lava flows of the lower succession have adakitic characteristics, including high Sr, low Y, low Yb, high Sr/Y, and high (La/Yb)_n. This likely reflects the influence of residual or fractionated amphibole in the ANS crust, rather than slab melting during active subduction. A post-collisional episode of delamination and heating of tonalitic lower crustal material, followed by mixing with asthenospheric mantle, created a primary magma with the characteristics of the Guruf basaltic andesite, including residual amphibole. There is no need for either late subduction in the area or long-term persistence of subduction-influenced material in the local convecting mantle.

 $\ensuremath{\mathbb{C}}$ 2021 Elsevier B.V. All rights reserved.

1. Introduction

The Arabian-Nubian Shield (ANS) (Fig. 1a) is part of the Pan-African belt, the largest known system of orogenies on Earth (Johnson and Woldehaimanot 2003). The ANS extends from Egypt in the west to Saudi Arabia in the east and from Jordan and southern Israel in the

* Corresponding author. E-mail address: babuamarah@ksu.edu.sa (B.A. Abuamarah). north to Eritrea and Ethiopia in the south. The ANS is a collage of Neoproterozoic ophiolites and juvenile arc terranes, younger sedimentary and volcanic basins, voluminous granitoid intrusions, and enclaves of pre-Neoproterozoic crust (Hargrove et al. 2006). Basement exposures of the ANS were exhumed in the Neogene by uplift associated with Red Sea rifting (Azer and Asimow, 2021).

Post-collisional magmatism in the northernmost ANS includes both intermediate to silicic plutonic bodies and numerous volcanic series. This vast magmatic phase commenced at ca. 635–625 Ma and

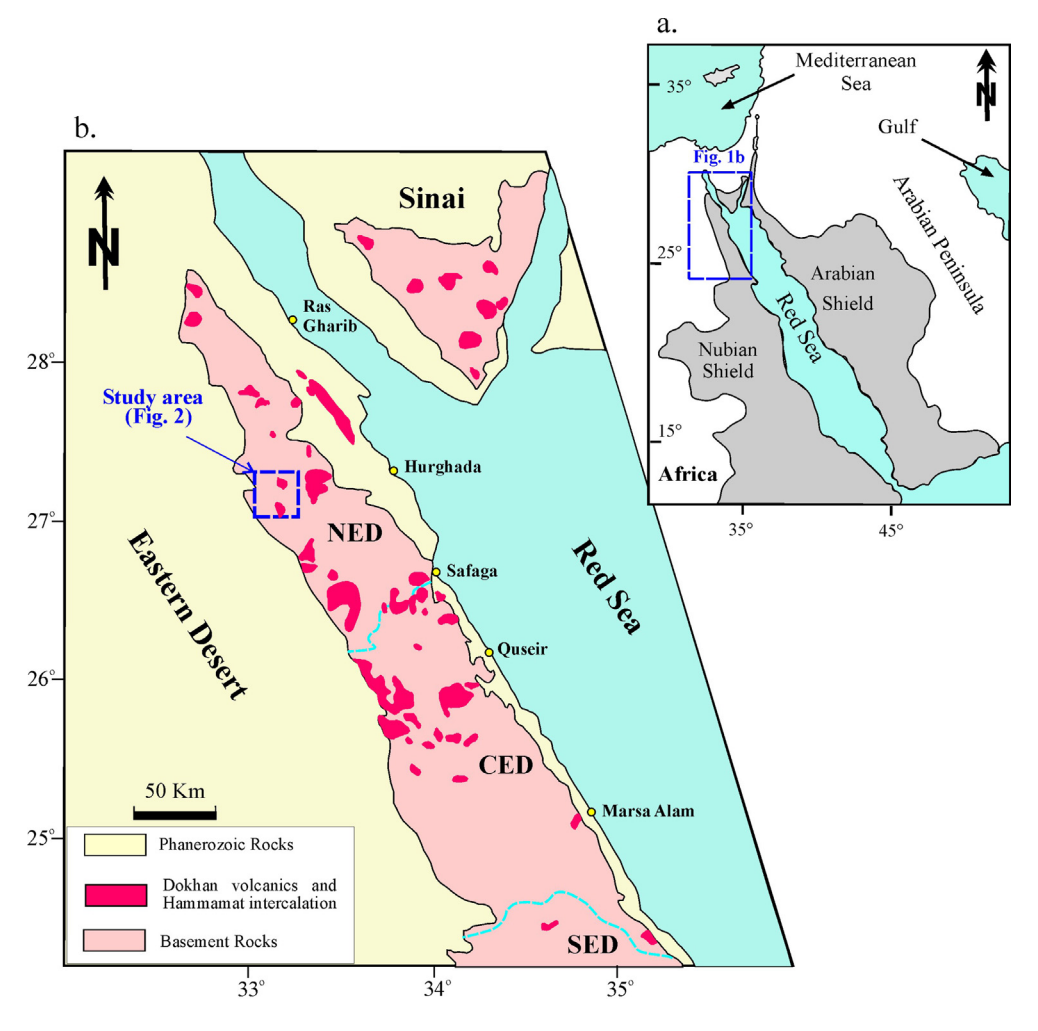


Fig. 1. (a) Index map of the Arabian-Nubian Shield showing the location of Fig. 1b; (b) Regional geological map of Egypt showing distribution of the Dokhan volcanics and Hammamat sediments in the Eastern Desert and Sinai, Egypt (modified after Abdel Rahman, 1996; Wilde and Youssef 2002). The location of the study area displayed in Fig. 2 is marked and the approximate boundaries between the north Eastern Desert (NED), central Eastern Desert (CED) and south Eastern Desert (SED) are shown as red dashed lines. (For interpretation of the references to color in this figure legend, the reader is referred to the web version of this article.)

culminated at 610-600 Ma. There was a transition (with some overlap in time) from batholithic calc-alkaline to alkaline A-type granite magmatism at ca. 600 Ma (Be'eri-Shlevin et al. 2011). The early postcollisional volcano-sedimentary sequences dominate in the northern part of the ANS, especially in the Eastern Desert and Sinai, where they are associated with clastic sedimentary deposits. In the Eastern Desert of Egypt, they are known as the Dokhan volcanics and dated at 630-590 Ma (Abu El-Enen et al. 2018; Breitkreuz et al. 2010; Wilde and Youssef 2000). They differ from the preceding arc metavolcanic sequences in the abundance of felsic varieties, their high potassium contents, the presence of ignimbrites, and the absence of metamorphism. The Dokhan volcanics include intermediate to felsic subaerial lava flows and their pyroclastic equivalents, as well as subvolcanic bodies and minor basalt and basaltic andesite. The Dokhan volcanics have been separated in many areas into lower and upper sequences (Breitkreuz et al. 2010: Obeid and Azer 2015).

In this work, we document a late Neoproterozoic volcanosedimentary succession exposed at Gabal (G.) Um Guruf, in the north Eastern Desert of Egypt. The calc-alkaline volcanic members of this succession (here named Guruf volcanics in order to accurately indicate their location) have been previously interpreted as subduction-related volcanism despite their young age compared to other evidence of subduction in the region (by Maurice et al. 2018, who named the section they studied after the nearby Wadi Hamad). Although, as we will see, the Guruf volcanics of the lower unit are calc-alkaline and show many typical features of subduction-related magmas, they do not show any evidence of metamorphism, which is a universal feature of the subduction-related volcanic phase in the ANS. We seek to resolve this issue and to interpret our new discovery of adakitic members of the volcanic series through detailed field work, mineralogical and geochemical investigations of the Guruf volcanics, and studies of the metavolcanic xenoliths in the adjacent granodiorite that clarify the relationship of the volcanic series to its country rocks. Based on the present results, we assign the Dokhan volcanics that outcrop at G. Um Guruf to the post-collisional phase of the ANS and their subduction-related characteristics to inheritance from earlier arc episodes rather than to active subduction, for which there is no other evidence in the region at this time.

2. Geologic setting

The Guruf volcano-sedimentary succession is exposed in the northern sector of the Eastern Desert, to the west of Hurghada town (Fig. 1b). The study area is bounded by latitudes 27° 06′ and 27° 16′ E and by longitudes 32° 57′ and 33°10′ N. The mapped area includes Neoproterozoic granitoids, calc-alkaline volcanic rocks and molasse (Hammamat) sedimentary units (Fig. 2). The area is dissected by many structurally controlled Wadis (W.). The granitoid rocks include

quartz-diorite, granodiorite and alkali feldspar granite. Published works on the study area have left unsettled substantial controversy about the geologic settings of the various rock units (Ali 2015; Basta et al. 2017; Maurice et al. 2018; Moussa et al. 2008).

Basta et al. (2017) concluded that all the granitoid rocks in the G. Um Guruf area are younger than the Dokhan volcanics and that all the granitoids were emplaced in a subduction-related tectonic setting, implying that the local Dokhan volcanics also date from an era of active subduction. However, our field observations of intrusive relations demonstrate that the granitoids in the study area can be divided into two different phases, separated by eruption of the local sequence of Dokhan volcanics. The early phase includes quartz diorite and granodiorite, while the later phase consists of alkali feldspar granite. The quartz-diorite and granodiorite are both medium-to-coarse-grained and form low hills with dark grey, grey, or whitish-grey color. They are extensively weathered, exfoliated, and exhibit cavernous weathering. The granodiorite contains

mafic microgranular enclaves (MMEs) and xenoliths of gneiss and porphyritic metavolcanic rocks. The MMEs are fine-grained and their shapes are ellipsoidal to irregular due to embayment of their margins. In places, their margins show evidence of hybridization or gneissic texture due to shear. The granodiorite is cut by many dikes of various compositions that abut against the Guruf volcanics and are cut by alkali feldspar granite. The previous studies concur with our observations of the intrusive relations, concluding that the quartz-diorite and granodiorite in the area are older than the Guruf volcanics (Hossny 2008). Basta et al. (2017) were compelled to adopt the opposite sequence on the basis of their assumption that the metavolcanic xenoliths in the quartz-diorite and granodiorite are derived from the Guruf volcanics, but they presented no evidence to support this interpretation. We sampled and characterized the gneiss and metavolcanic xenoliths in the granodiorite in order to test the conclusion of Basta et al. (2017) and resolve the question of relative chronology.

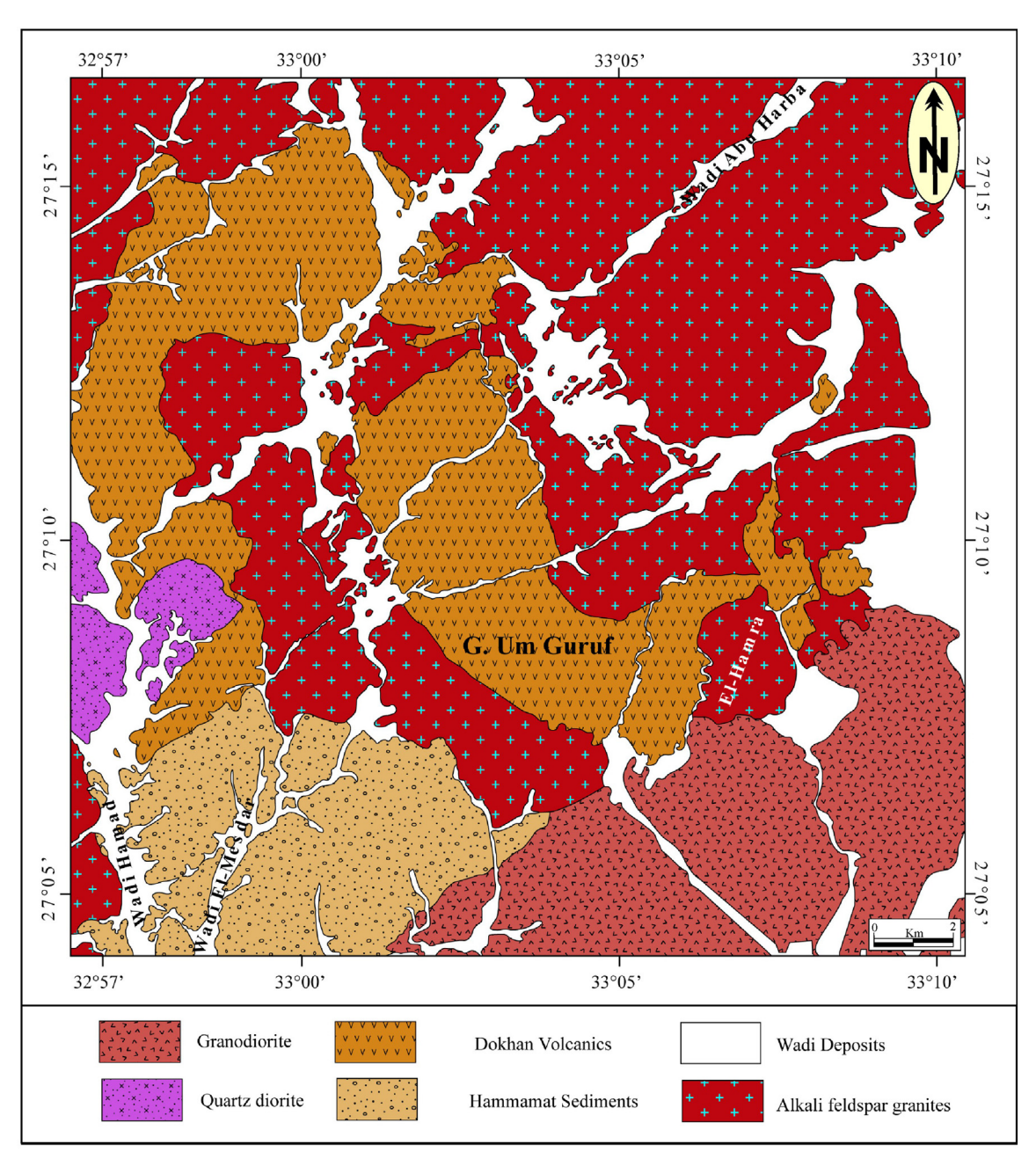


Fig. 2. Geologic map of Gabal Um Guruf area, North Eastern Desert, Egypt (modified after Basta et al. 2017).

The Guruf volcanic rocks are exposed mainly around *G*. Um Guruf and to the northwest, across W. Hamad. Although outcrop is discontinuous, they apparently represent a western extension of the Dokhan volcanics from their type locality at Gabal Abu Dokhan, which lies immediately east of the study area. They extruded onto and unconformably overlie the quartz-diorite and granodiorite with sharp contacts (Fig. 3a), whereas they are truncated and intruded by alkali feldspar granite (Fig. 3b).

The Guruf volcanic rocks show a range of colors in the field: dark grey to grey, greenish-grey, and reddish-brown. They form part of an interlayered volcano-sedimentary series that can be divided into upper and lower successions of lava flows intercalated with pyroclastic rocks. The lower succession consists of basaltic andesite, andesite and

dacite, while the upper succession consists of rhyodacite, rhyolite and ignimbrite. Outcrops of the upper succession are limited and are well exposed only east of the G. Um Guruf mass; there are few exposures in the western part of the study area along W. Hamad. There is a clear angular unconformity between the upper and lower successions (Fig. 3c). Pyroclastic deposits (agglomerates, ignimbrites and tuffs) alternate with the lava flows in both the upper and lower successions. Again, a well-defined angular unconformity can be observed where tilted pyroclastic deposits of the upper sequence rest on nearly flatflying lava flows of the lower sequence (Fig. 3d). Maurice et al. (2018) focused their discussion of the Dokhan volcanic rocks of the W. Hamad area exclusively on andesites and dacites, despite reporting numerous rhyolitic and rhyodacitic analyses.

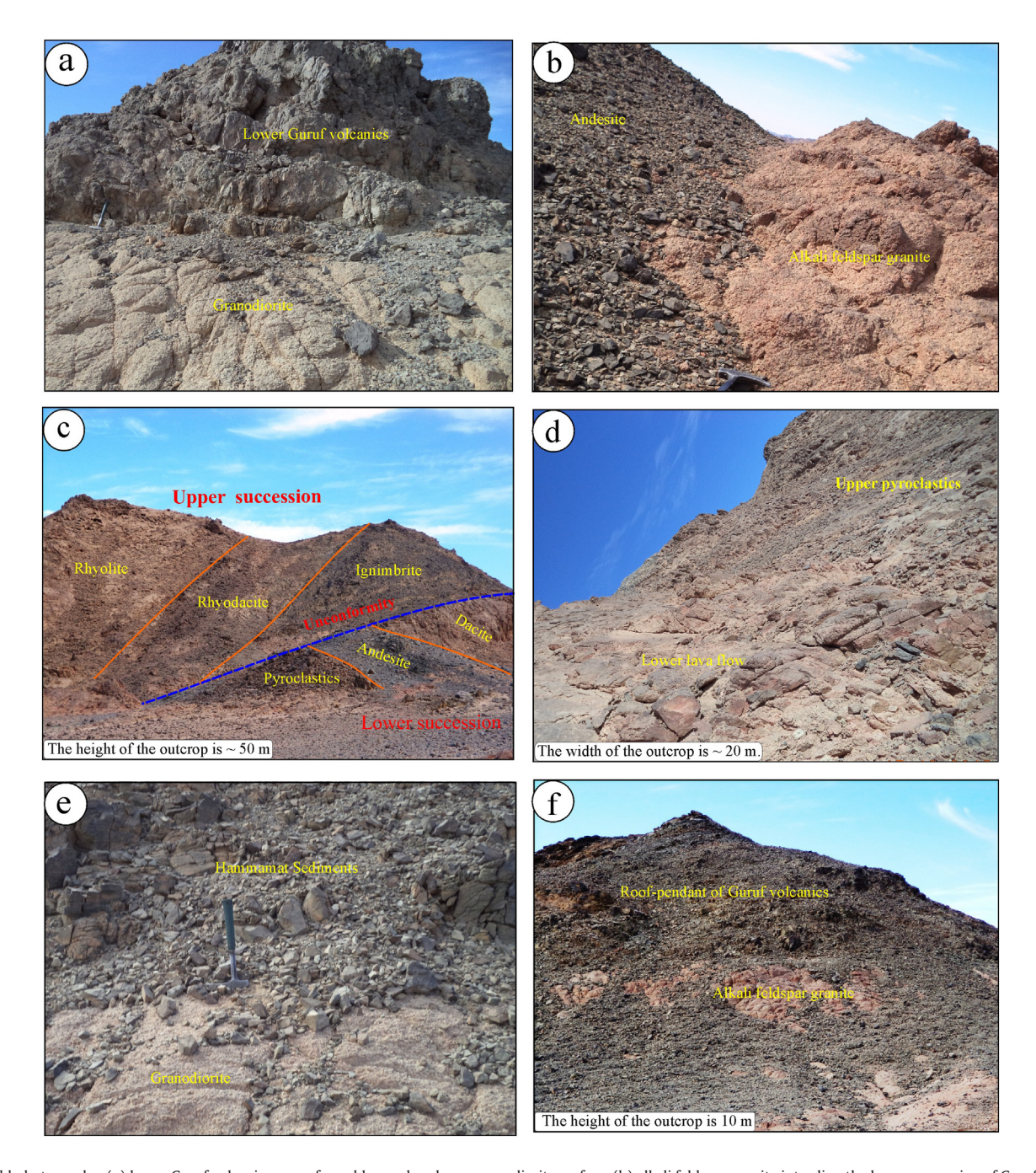


Fig. 3. Field photographs: (a) lower Guruf volcanics unconformably emplaced on a granodiorite surface, (b) alkali feldspar granite intruding the lower succession of Guruf volcanics, (c) upper Guruf volcanics unconformably resting on the lower succession, (d) titled pyroclastic beds of the upper cycle unconformably resting on the lower lava flows, (e) Hammamat sediments deposited nonconformably on a granodiorite surface, and (f) a roof-pendant of the Guruf volcanics above alkali feldspar granite.

The Hammamat molasse-type sedimentary rocks are exposed in the southwestern part of the mapped area. They vary in color from greenish-grey to brick red. They are deposited directly on a paleosurface of granodiorite with a basal conglomerate (Fig. 3e) or intercalated with the Guruf volcanics. They consist of alternating beds of mostly conglomerate and greywacke, with less common siltstone and mudstone.

The alkali feldspar granites are the most abundant rocks in the mapped area; they include more than one intrusive phase (Basta et al. 2017). These granites are the youngest igneous activity in the mapped area; field observations demonstrate that they intruded into both granodiorite and Guruf volcanics; off-shoots of the alkali feldspar granite are observed in the Guruf volcanics and xenoliths of both granodiorite and Guruf volcanics are enclosed in alkali feldspar granite near their contacts. The alkali feldspar granites are massive, medium-to coarse-grained, and pink to red in color. Unlike the quartz diorite and granodiorite, the alkali feldspar granites are devoid of mafic microgranular enclaves or dikes. Some roof-pendants of Guruf volcanics above alkali feldspar granite were noted (Fig. 3f). In some places, pegmatite and fluorite veins occur along contacts between the alkali feldspar granites and their country rocks.

Two generation of dikes are recognized in the study area. The first group (calc-alkaline dikes) cuts quartz-diorite and granodiorite but is truncated by both Guruf volcanics and alkali feldspar granites. The second group (alkaline dikes) cuts quartz-diorite, granodiorite and Guruf volcanics, but is intruded by alkali feldspar granites.

There are some age constraints for the granitoids. The U—Pb zircon age of alkali feldspar granites just to the north of the study area at G. Abu Marwa is 595 \pm 8.5 Ma (Ali 2015), consistent with a Rb—Sr whole-rock age of 590 \pm 4 Ma for the same granites (Moussa, 1998). Likewise, Moussa et al. (2008) obtained an age of 595.3 \pm 3.3 Ma for alkali feldspar granite at G. Abu Harba, just at the NE border of the present mapped area. The U—Pb zircon age of alkali feldspar granite at G. El-Glouf (the SW corner of the mapped area) is 596.4 \pm 11.2 Ma (Ali 2015). These dated granitoids intrude the Guruf volcanics, which are therefore older than ~595 Ma. There is no formal upper bound on the maximum age of the Guruf volcanics, as the local granodiorite and quartz diorite have not been dated. Although U-Pb zircon dates are available for a number of ignimbrites associated with Dokhan volcanics in the Eastern Desert (e.g., Breitkreuz et al. 2010), none of them are within the current study area and we do not assume any correlation to other dated sections.

3. Petrography

This section will describe in detail the petrography of the Guruf lava flows (basaltic andesite, andesite, dacite, rhyodacite and rhyolite), their associated pyroclastic deposits (ignimbrite, agglomerates, lapilli tuffs, crystal tuffs and banded tuffs), the two types of dikes, and the metavolcanic xenoliths in the granodiorite.

3.1. Lava flows

3.1.1. Lower Guruf volcanics

The lower lava flows of the Guruf volcanic series include basaltic andesite, andesite and dacite. Basaltic andesite is porphyritic, with abundant plagioclase and clinopyroxene phenocrysts set in a fine-grained groundmass of plagioclase, clinopyroxene, and abundant (~8 vol%) opaque minerals. Accessory phases include apatite and titanite; secondary minerals include chlorite, actinolite, sericite and veinlets of quartz and epidote. Plagioclase phenocrysts are generally twinned, rarely zoned, and slightly altered to sericite; small plagioclase laths in the groundmass show a clear preferred orientation (Fig. 4a). Clinopyroxene forms anhedral microphenocrysts of augite (Fig. 4b), partly replaced by secondary amphibole and chlorite. Some augite phenocrysts show oscillatory or reverse zoning, confirmed by microprobe analyses.

Andesite is massive, fine-grained and greenish to reddish-grey. It is commonly porphyritic and consists of abundant plagioclase and subordinate amphibole and clinopyroxene phenocrysts set in a fine-grained groundmass. Some andesite samples contain amygdales filled with secondary minerals. Accessory phases include opaques and apatite; sericite, calcite and chlorite are secondary. Some plagioclase crystals are saussuritized; others show prominent oscillatory zoning (Fig. 4c). Equant microphenocrysts of augite may display irregular edges suggesting partial resorption or replacement around their margins by tremolite, chlorite, and iron oxides. Primary amphibole forms subhedral to euhedral, elongated phenocrysts that are simply twinned and rarely zoned. The groundmass displays shape-preferred alignment and is composed of plagioclase laths, amphibole, biotite, augite and opaques.

Dacite is massive, fine-grained and pinkish-grey. It carries abundant subhedral to euhedral plagioclase phenocrysts up to 3.0 mm long, together with scarce biotite, amphibole and quartz microphenocrysts, set in a microcrystalline felsic groundmass. Apatite, zircon and Fe—Ti oxides are the common accessory phases, while epidote, sericite and chlorite are present as secondary minerals. The plagioclase phenocrysts are subhedral to euhedral tabular crystals showing complex zoning (Fig. 4d). Some plagioclase phenocrysts are slightly to moderately altered to sericite and epidote. Subhedral tabular microphenocrysts of biotite are slightly altered to chlorite and opaques. A few small crystals of altered amphibole and of quartz are observed in some samples.

3.1.2. Upper Guruf volcanics

The lava flows of the upper Guruf volcanic series include rhyolite and rhyodacite. Rhyolite is fine-grained with 10–25% phenocrysts set in microcrystalline groundmass. The phenocrysts mostly occur as discrete crystals but rare glomerophyric or cumulophyric aggregates are present. The phenocrysts include plagioclase, K-feldspar and quartz with rare microphenocrysts of biotite and pyrophanite. Biotite occurs as tabular corroded crystals (Fig. 4e). Pyrophanite is recorded for the first time in the post collisional calc-alkaline volcanics in Egypt. It is an opaque member of the ilmenite group with formula MnTiO₃ and crystallizes in the trigonal system. It occurs as anhedral to subhedral microphenocrysts associated with apatite and zircon (Fig. 4f). The groundmass is microcrystalline and shows microgranular and spherulitic textures. The textures of these rhyolite samples definitively indicate emplacement as a lava flow; there are not pyroclastic rocks.

Rhyodacite is observed only in the upper series of the Guruf volcanics. It is rather similar to the dacite in the lower series but contains more K-feldspar and quartz phenocrysts and a lower abundance of mafic minerals. Phenocrysts in rhyodacite, either as discrete crystals or glomerophyric aggregates, vary significantly in modal abundance and are set in microcrystalline groundmass. Phenocryst phases include plagioclase, K-feldspar, and quartz with rare microphenocrysts of biotite. Again, these rhyodacite samples were emplaced as flows; they are not pyroclastic.

3.2. Pyroclastic deposits

The pyroclastic rocks are recognized and distinguished from the lavas by their textures. Their nomenclature and classification is purely descriptive and based primarily on their granulometric state. Pyroclastic rocks occur in both lower and upper units; they include ignimbrite, agglomerate, and several varieties of tuff (lapilli tuff, crystal tuff, and banded tuff).

Ignimbrites, both welded and unwelded, are abundant in the upper succession, associated with rhyolite. They are rhyolitic in composition and show a foliation defined by flattened lenticular glass particles (fiamme) in a groundmass of felsic volcanic glass, pumice, and irregular glass shards. The fiamme may be sinuously curved or flattened; their preferred orientation is attributed to compaction and welding. The groundmass shows fluidal structure and encloses crystals, crystal fragments, and scarce felsic rock fragments with various degrees of welding.

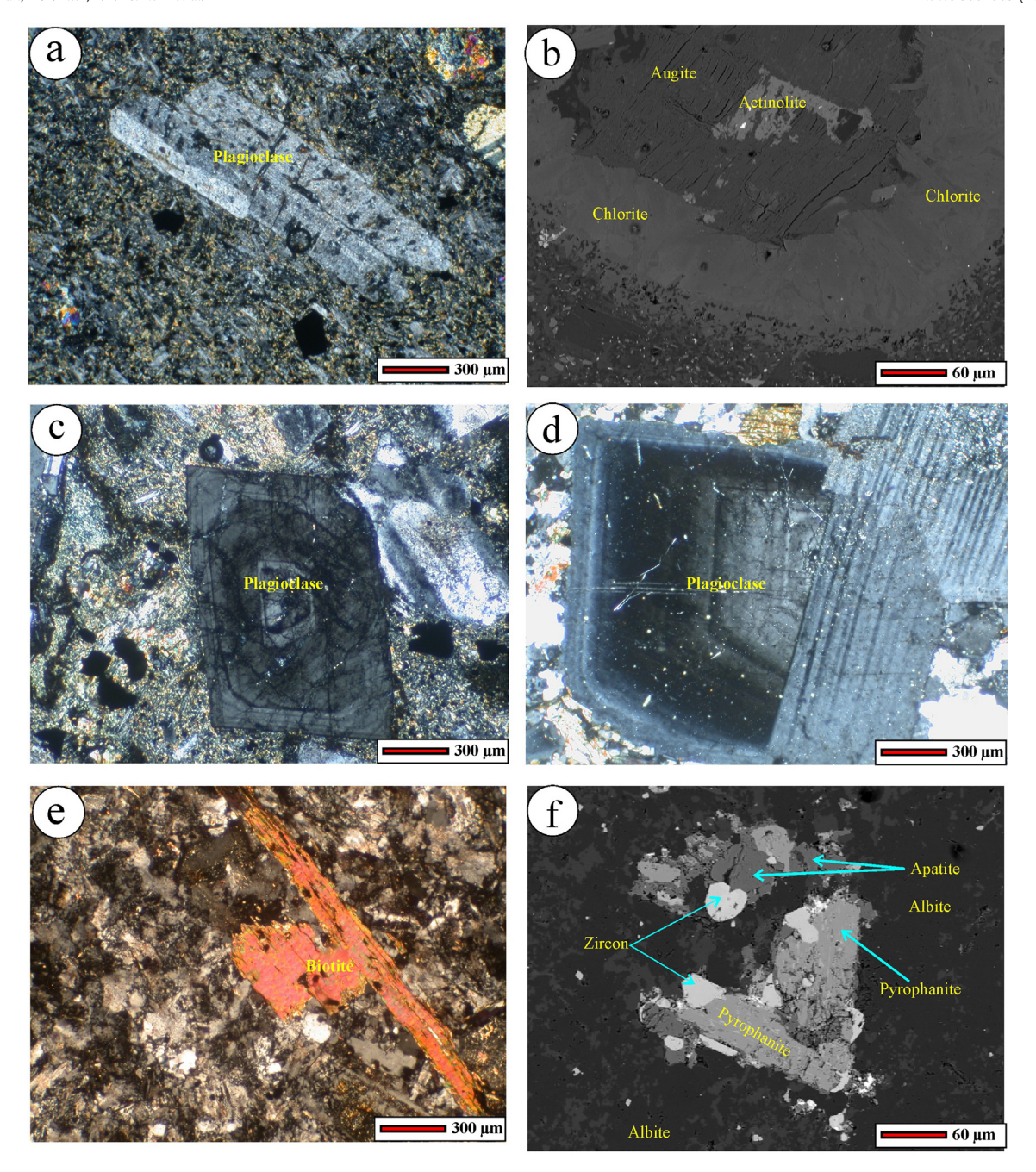


Fig. 4. Photomicrographs showing petrographic textures in cross-polarized transmitted light (a, c, d and e) or back-scattered electrons (b and f): (a) large plagioclase phenocryst embedded in groundmass showing flow texture in basaltic andesite, (b) phenocryst of clinopyroxene marginally altered to chlorite in basaltic andesite, (c) plagioclase phenocryst show oscillatory zoning in andesite, (d) plagioclase phenocryst showing complex zoning in dacite, (e) microphenocryst of biotite embedded in felsic groundmass in rhyolite, and (f) microphenocrysts of pyrophanite associated with apatite and zircon.

Rarely, groundmass shows spherulitic texture and devitrification into equigranular mosaic crystal aggregates.

Agglomerates are poorly sorted rocks assembled from rounded to subrounded volcanic 3–6 cm rock fragments embedded in a glassy to tuffaceous groundmass. The rock fragments are volcanic, including porphyritic andesite and dacite with rare basaltic andesite. Some coarse crystal fragments of altered mafic minerals, plagioclase, K-feldspars, and quartz are observed in the groundmass. The groundmass consists of glassy tuff, small lithic and crystal fragments, and abundant stretched vesicles filled with secondary minerals such as quartz, carbonates, adularia and epidote.

Lapilli tuffs are composed of angular to subangular crystal and lithic fragments set in fine tuffaceous groundmass. They are poorly sorted,

with pyroclast sizes extending from 3 to 45 mm. The lithic fragments include andesite, dacite and rhyolite, all with porphyritic textures. The crystal fragments are mainly cracked crystals of plagioclase, altered mafic minerals, and quartz with lesser opaque minerals and rare K-feldspars. The matrix may be glassy or may consist of fine plagioclase and quartz fragments with minor opaque minerals.

Crystal tuffs are composed predominantly of crystal fragments of variable sizes, embedded along with minor rock fragments in a glassy or fine tuffaceous groundmass. The crystal fragments include plagioclase, quartz and mafic minerals. The plagioclase and mafic minerals crystal fragments are highly altered. Rare angular lithic (andesite to rhyolite) and glass fragments of variable sizes are present.

Banded tuffs are very fine-grained. They are composed of alternating laminae (< 2.0 mm thick) and thin beds (< 10 mm thick) of variable color, reflecting changes in grain size and composition. The fine laminae consist of very fine-grained, vitreous-ashy material, with tiny particles of quartz and feldspars. The thin beds contain coarser crystals and crystal fragments of plagioclase and quartz with rare altered mafic minerals set in a sericite-rich groundmass.

3.3. Dikes

3.3.1. Calc-alkaline dikes

The calc-alkaline dikes in the study area include basalt, andesite and rhyolite. Basalt dikes are fine-grained and include porphyritic, subophitic and rarely doleritic varieties. Phenocrysts of plagioclase, hornblende and clinopyroxene are embedded in a fine-grained to microcrystalline groundmass of plagioclase, augite and magnetite with minor secondary epidote and chlorite. Accessory phases include opaques and apatite; chlorite, actinolite, sericite and titanite are secondary. Subhedral zoned plagioclase is the dominant phenocryst. Hornblende forms euhedral to subhedral phenocrysts and small prisms in the groundmass; it variably altered to chlorite. Clinopyroxene displays different habits, from phenocrysts to small interstitial grains; it is sometimes replaced by amphibole.

Andesite dikes are massive, fine-grained and reddish-grey. They consist essentially of plagioclase and hornblende phenocrysts with micro-phenocrysts of augite in a fine-grained groundmass. Accessory opaque minerals and apatite are present, as well as secondary sericite, calcite and chlorite. The groundmass is composed of subhedral to anhedral plagioclase laths, up to 0.3 mm long, along with hornblende, quartz, and opaques.

Rhyolite dikes are fine-grained, with variable phenocryst abundances (<30%) and microcrystalline groundmass. The phenocrysts occur as discrete crystals and as glomerophyric or cumulophyric aggregates. Phenocrysts include plagioclase, K-feldspar and quartz with rare microphenocrysts of biotite. The groundmass is microcrystalline and shows microgranular and spherulitic textures.

3.3.2. Alkaline dikes

Alkaline dikes in the study area include trachyandesite and alkali rhyolite. Trachyandesite dikes are porphyritic, with phenocrysts of plagioclase, clinopyroxene and amphibole in a fine-grained groundmass of the same minerals along with accessory opaques and apatite. Plagioclase forms both tabular phenocrysts and fine-grained laths in the groundmass. Hornblende forms both large prismatic crystals and granular aggregates. Clinopyroxene, mainly augite, is present as euhedral to subhedral prismatic phenocrysts and granular aggregates in the groundmass.

Alkali rhyolite dikes are porphyritic and composed mainly of alkali feldspar phenocrysts in a fine-grained groundmass. Alkali feldspar is mostly turbid and stained reddish-brown. Quartz occurs as small anhedral microphenocrysts and in the groundmass. The mafic minerals are difficult to distinguish as they are highly altered to chlorite and iron oxides. The groundmass shows trachytic texture defined by aligned alkali feldspar laths and altered mafic microlites. Apatite and zircon are the main accessory minerals; chlorite, epidote and calcite are the main secondary minerals.

3.4. Metavolcanic xenoliths

Metavolcanic xenoliths in granodiorite include metabasalt and meta-andesite. Metabasalt is porphyritic and fine-grained, massive, and dark greenish-grey to black. It is composed essentially of plagioclase, augite and amphibole phenocrysts in fine-grained groundmass of plagioclase and augite with accessory titanite, apatite, and opaque minerals. Subhedral to euhedral plagioclase crystals are partly to completely altered to epidote and sericite but zoning can be recognized

in the relict fresh plagioclase. Some plagioclase phenocrysts show bent twin planes due to deformation. Amphibole is highly altered to actinolite, chlorite, and opaques. Augite occurs as subhedral prismatic crystals that occasionally show simple twinning.

Meta-andesite is porphyritic and fine-grained, massive, and grey to greenish-grey. The phenocrysts include plagioclase, pyroxene, amphibole and opaques in fine-grained groundmass of the same minerals as well as accessory zircon and titanite. Actinolite, epidote, calcite, and chlorite are secondary. Plagioclase phenocrysts occur as large subhedral to euhedral tabular crystals highly altered in the cores to epidote and sericite. Augite is found as individual large phenocrysts and as fine crystals in the groundmass.

4. Analytical methods

Based on the petrographic studies, 42 rock samples (29 lava flows, 10 dikes and 3 volcanic xenoliths) were analyzed for major, trace and rare earth elements at Activation Laboratories Ltd. (Actlabs, Canada) and the California Institute of Technology (Caltech, USA). In the Actlabs (Canada) analyses, the major oxides were measured by lithium metaborate/tetraborate fusion ICP-AES. Trace and rare earth elements were measured by ICP-MS following lithium borate fusion and acid digestion. Loss on ignition (LOI) is determined by weight difference after ignition at 1000 °C. Precision and accuracy were controlled by analysis of international reference materials and replicate analyses and are 1% for major elements and 2% to 5% for trace elements. Full details are on the laboratory website (actlabs.com).

At Caltech, whole-rock compositions of major and minor elements were determined using a Panalytical Zetium wavelength-dispersive XRF spectrometer. Sample powders were milled in an agate ball mill and loss on ignition (LOI) determined by weighing before and after firing in air for 1 h at 1050 °C for mafic samples and at 1000 °C for felsic samples. Fused-glass beads were prepared from fired powders by mixing with 10 times their weight in 66.67% Li₂B₄O₇-32.83% LiBO₂-0.50% LiI flux and fusing at 1200 °C. The XRF protocol was calibrated against 21 USGS rock standards. USGS standards BCR-2, AGV-2, and RGM-2 (a basalt, an andesite, and a rhyolite) were routinely analyzed along with unknowns for quality control and drift correction. After XRF measurement, 25 ± 1 mg chips of the fused-glass beads were dissolved in new 50 mL polypropylene tubes by refluxing in 2 mL of hot (100 °C) 3:1 nitric and hydrofluoric acid for at least 8 h. After dilution with milli-Q distilled water to 30 mL total volume, elemental concentrations of rare earth elements (REE) and selected major and trace elements were determined with an Agilent Technologies 8800 triple quadrupole ICP-MS. A working curve for instrument sensitivity was developed using a blank fused bead from the same batch of flux along with USGS standards AGV-2 and RGM-2. To control for quality, additional USGS standards (DTS-2, BCR-1, G-2) were included as unknowns.

Mineral chemical analyses, electron backscatter images, and X-ray mapping were obtained with a five-spectrometer JEOL JXA-8200 electron microprobe at Caltech. Surfaces were coated with ~15 nm of carbon. Operating conditions were 15 kV, 25 nA, 1 μm beam, 20 s onpeak counting times, the mean atomic number (MAN) background-correction method, and the CITZAF matrix correction routine. The analytical standards used for analyses were synthetic forsterite, fayalite, Mn-olivine, anorthite, TiO2, and Cr2O3; Amelia albite, Asbestos microcline, and Durango apatite. Quartz, MgO, and Al2O3 provided additional control points for the MAN background subtraction.

5. Mineral chemistry

Compositions of the essential minerals (pyroxene, amphiboles, feld-spars, chlorite, pyrophanite, and Fe—Ti oxides) were analyzed in basaltic andesite, andesite, dacite and rhyolite. Most analyses were performed on phenocrysts or microphenocrysts large enough for

single-phase analyses. All the microprobe data are presented as an online supplement (Tables 1SD-9SD).

Chemical compositions, structural formulae and end-member components of pyroxene phenocrysts in basaltic andesite and andesite are given in Supplementary Table 1SD. All pyroxene analyses are rich in CaO and classify mainly as augite according to Morimoto et al. (1988) (Fig. 5a). Compositional variation, whether among crystals or within zoned phenocrysts, extends parallel to isotherms in the pyroxene quadrilateral projection. On the SiO₂ versus Al₂O₃ diagram of Le Bas (1962), all clinopyroxene analyses plot well into the subalkaline field (Fig. 5b).

Amphiboles, both primary and secondary (replacing clinopyroxene), were analyzed in basaltic andesite, andesite and dacite. Oxide analyses and structural formulae are given in Supplementary Table 2SD. Primary amphibole is high in TiO $_2$ (>1.0 wt%), whereas secondary amphibole has low TiO $_2$ (<0.5 wt%). All the amphibole analyses are calcic; primary amphibole ranges from magnesio-hornblende to tschermakitic hornblende, whereas secondary amphibole ranges from actinolite to actinolitic hornblende. The discrimination diagram of Keeditse et al. (2016) supports the petrographic interpretation that both primary and secondary amphibole is present in all rock types (Fig. 5c).

The analyzed feldspars include plagioclase, albite and K-feldspars. Their oxide compositions, structural formulae and end-member components are given in Supplementary Tables 3SD, 4SD and 5SD. Plagioclase

phenocrysts from basaltic andesite, andesite, and dacite show CaO contents decreasing as expected with petrographic type: andesine to labradorite (An₄₁₋₆₂) in basalt andesite, oligoclase to labradorite (An₁₄₋₅₃) in andesite, and oligoclase to andesine (An₁₁₋₃₆) in dacite. Where zoning was identified in basaltic andesite and andesite, it may be normal (decreasing An content towards rim) or oscillatory. Albite, An_{<8.4}, was analyzed only in dacite and rhyolite. K-Feldspars were analyzed in dacite and rhyolite; K₂O contents are high (14.6–16.1 wt% in dacite and 15.7–16.3 wt% in rhyolite) and CaO contents are low (<0.6 wt%). Perthitic exsolution was not observed in any of the samples.

Chlorite formed by replacement of pyroxene, biotite and amphibole; compositions and structural formulae of chlorite on the basis of 28 oxygens are given in Supplementary Table 6SD. Adopting the nomenclature of Hey (1954), most analyses are pycnochlorite, with minor extension into the neighboring fields of diabantite, ripidolite and brunsvigite (Fig. 5d). No particular correlation was noted between chlorite composition and which mafic mineral it replaced.

Pyrophanite, a member of the ilmenite group with end-member formula MnTiO₃, was identified in the rhyolite. The compositions, structural formulae and end-member components are given in Supplementary Table 7SD. Pyrophanite analyses are principally TiO₂ (45.4–51.7 wt%), FeO* (14.0–22.5 wt%) and MnO (28.8–33.4 wt%), corresponding to 62.8–72.0 mol% pyrophanite component. A single

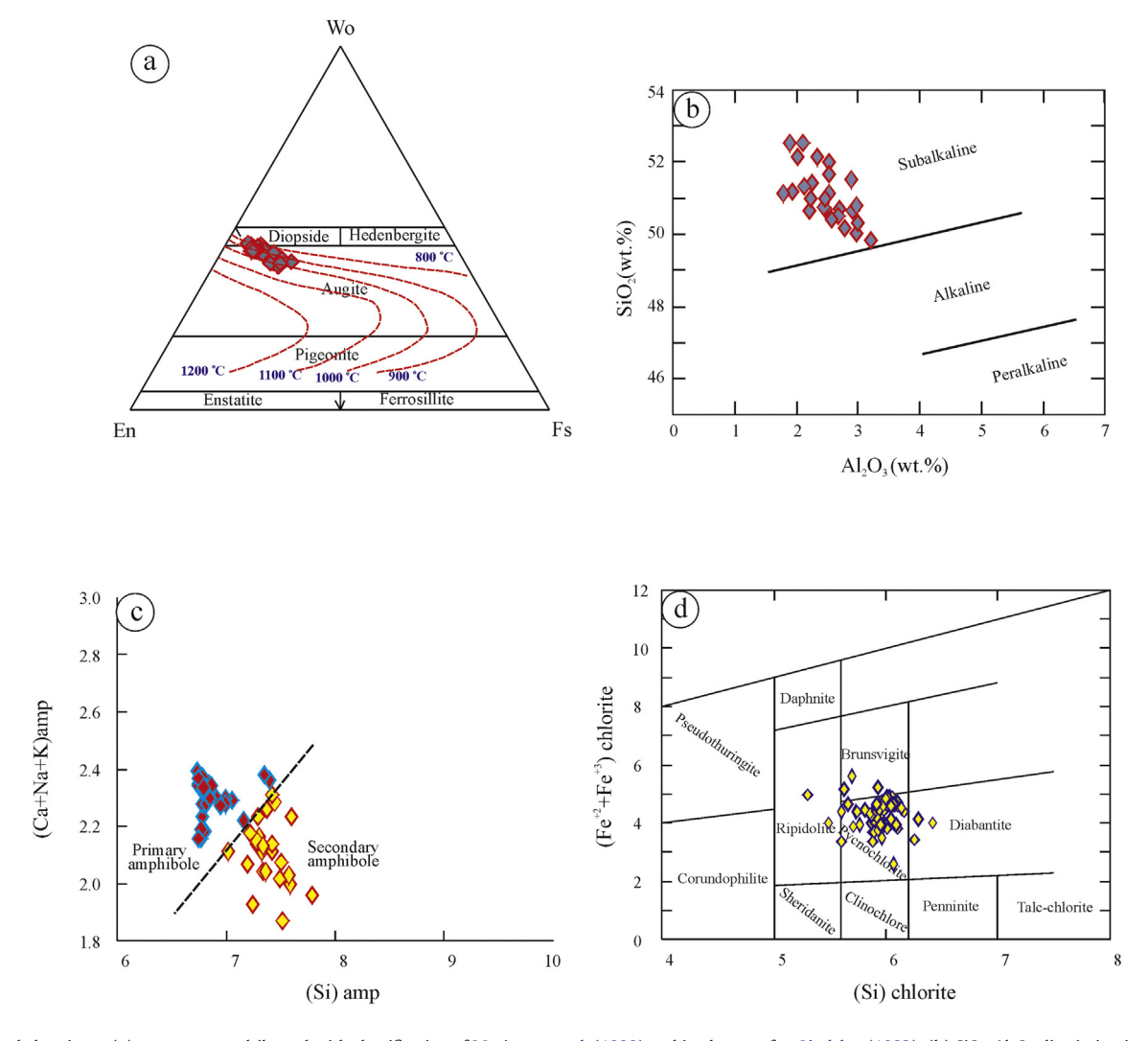


Fig. 5. Mineral chemistry: (a) pyroxene quadrilateral with classification of Morimoto et al. (1988) and isotherms after Lindsley (1983), (b) SiO₂-Al₂O₃ discrimination diagram for clinopyroxene (after Le Bas 1962), (c) discrimination diagram for primary and secondary amphiboles (after Keeditse et al. 2016), and (d) chlorite nomenclature (after Hey, 1954).

analysis of mixed ilmenite-series solid solution has subequal proportions of pyrophanite, ilmenite, and hematite components; it is probably altered material.

Fe—Ti oxides were analyzed in basaltic andesite, andesite, dacite and rhyolite. Magnetite and ilmenite are most common, with rare hematite and rutile considered to be alteration products. Chemical compositions, structural formulae and end-member components of magnetite and ilmenite are given in Supplementary Tables 8SD and 9SD. The magnetite in dacite is nearly homogenous, with low TiO2 contents (0.1–0.8 wt%; ≤ 2.2 mol% ulvöspinel). Magnetite in andesite and basaltic andesite mostly contains elevated TiO₂ contents (2.0-24.1 wt%, 6–73 mol% ulvöspinel) together with a small population of Ti-poor magnetite (<1.5 wt% TiO₂, ≤4 mol% ulvöspinel). Reflected light observations show coexisting homogeneous or exsolved titanomagnetite together with Ti-poor magnetite in andesite and basaltic andesite. Analyzed ilmenite is close to nominal end-member ilmenite (89-94 mol% FeTiO₃). It is notably poor in Al₂O₃, MgO and CaO. Ilmenite in dacite is enriched in MnO (3.3-3.4 wt%) compared to that in andesite (2.8-3.1 wt%) and basaltic andesite (1.3-2.9 wt%), as expected from progressive differentiation of calk-alkaline rocks under relatively oxidizing conditions.

6. Geochemistry

Twenty-nine lava samples (4 basaltic-andesite, 8 andesite, 5 dacite, 4 rhyodacite and 8 rhyolite) were selected for chemical analyses.

Three samples of metavolcanic xenoliths in the granodiorite were analyzed to test whether their protoliths were associated with the calcalkaline Guruf volcanics (Basta et al. 2017) or with the older island-arc volcanic phase in the region (Shadli metavolcanics). Moreover, 10 dike samples, associated with the studied volcanic series or cutting the country rocks, were analyzed to clarify the genetic relationships between the dikes and the volcanic units.

6.1. Geochemical characteristics

6.1.1. Lava flows

Major and trace element analyses of 29 new lava flow samples (Tables 1 and 2) are considered alongside 65 lava flow and pyroclastic analyses from other outcrops of the same volcanic sequences published by Maurice et al. (2018). The new analyses span a wide range of compositions (52.0–74.7 wt% SiO₂). On the total alkali-silica (TAS) diagram (Cox et al. 1979), the lower unit ranges from basaltic-andesite through andesite to dacite, while the upper unit is restricted to rhyolite (the category rhyodacite is not used on this diagram) (Fig. 6a). The Guruf volcanics straddle the dividing line between calc-alkaline and alkaline fields. The SiO₂ vs. Zr/TiO₂ diagram of Winchester and Floyd (1977) gives consistent results, with the new Guruf volcanic data spanning the subalkaline andesite, dacite, rhyodacite and rhyolite fields (Fig. 6b). Maurice et al. (2018) applied the term Dokhan volcanics only to andesite and dacite (plus minor basalt and basaltic andesite), despite publishing numerous analyses of rhyodacite and rhyolite (Fig. 6 a,b). The Guruf

Table 1Chemical composition of the lower lava flows of Guruf volcanics, North Eastern Desert, Egypt.

Rock type	Basaltic	andesite			Andesit	e							Dacite					
Sample	GH22	GH23	GH26	GH27	GH28	GH30	GH31	GH32	GH33	GH34	GH35	GH36	GH2 ^a	GH3 ^a	GH13 ^a	GH24	GH25	GH29
SiO ₂	52.05	54.19	54.88	53.75	56.48	56.16	58.7	57.7	60.93	57.44	61.36	57.22	65.23	62.454	66.07	64.36	63.73	63.92
TiO ₂	1.48	1.35	1.51	1.4	1.35	1.39	1.39	1.13	1.05	1.16	0.99	1.2	0.61	0.624	0.48	0.98	0.87	0.88
Al_2O_3	17.82	17.33	15.53	17.3	16.63	16.92	16.03	16.56	15.3	16.38	15.86	15.76	15.72	16.380	14.20	14.12	15.95	16.02
Fe_2O_3	8.04	8.09	8.29	7.74	6.94	7.38	6.1	7.86	6.71	6.99	5.97	7.65	3.11	4.291	3.63	6.24	4.7	4.67
MnO	0.13	0.12	0.16	0.15	0.11	0.11	0.11	0.11	0.08	0.09	0.06	0.12	0.12	0.122	0.06	0.09	0.07	0.06
MgO	4.93	4.88	4.75	4.27	3.51	3.69	3.29	3.39	2.92	3.03	3.04	3.74	0.97	1.647	1.97	2.63	2.58	2.25
CaO	6.29	6.51	5.59	6.7	4.87	4.81	5.14	4.75	4.66	4.91	3.77	5.76	1.83	3.464	2.27	2.8	3.85	3.72
Na_2O	3.81	3.72	5.23	4.12	4.92	4.91	4.27	3.96	3.53	4.23	4.1	3.27	6.35	4.474	3.69	4.15	4.32	4.21
K ₂ O	1.55	1.38	1.6	1.56	2.14	2.07	2.4	2.41	2.52	2.45	2.73	2.02	2.77	3.116	3.95	2.87	2.9	3.07
P_2O_5	0.53	0.49	0.45	0.53	0.39	0.37	0.39	0.32	0.3	0.34	0.29	0.39	0.15	0.203	0.13	0.19	0.24	0.33
LOI	2.92	1.23	1.22	2.21	1.83	1.55	1.61	1.81	0.98	2.31	1.6	2.19	0.39	0.891	1.03	1.18	1.07	1.1
Total	99.55	99.29	99.21	99.73	99.17	99.36	99.43	100	98.98	99.33	99.77	99.32	97.24	97.666	97.50	99.61	100.28	100.23
Sc	16.99	20.48	16.96	17.35	14.54	14.96	11.09	14.49	9.54	13.07	8.62	13.20	3.28	5.16	1.99	8.72	16.67	17.62
Rb	31.19	25.96	41.93	30.86	35.98	34.22	40.24	58.51	45.10	41.94	54.41	23.41	80.82	118.75	101.14	64.64	52.50	46.65
Ba	630.93	519.52	648.63	649.56	744.21	666.50	809.39	701.25	1113.69	811.77	1098.16	978.24	1393.33	768.45	856.74	989.83	674.08	605.21
Sr	971.66	901.66	855.72	825.17	862.56	769.41	889.33	852.15	826.44	872.36	660.71	827.36	295.33	527.31	360.17	606.04	675.46	732.35
Nb	6.63	5.08	7.51	7.45	7.25	7.95	8.10	6.10	6.44	6.05	6.68	9.67	13.24	9.30	7.22	6.20	9.24	8.91
Zr	161.10	117.74		164.94	165.25	177.71	226.45	151.99	168.53	158.77	205.88	271.84	318.63	215.61	153.97	175.92	175.54	234.52
Hf	3.65	3.09	4.42	4.33	4.20	4.53	5.22	3.88	5.83	3.95	6.23	4.84	8.37	5.19	4.17	7.68	5.40	5.38
Y	14.18	9.88	13.46	16.69	16.83	18.26	17.46	15.85	13.81	13.49	13.70	16.21	29.55	20.59	15.06	16.35	15.81	16.28
Zn	76.25	75.50	92.04	74.73	66.70	70.28	66.02	62.05	53.79	66.70	61.65	113.47	61.99	61.10	44.77	51.73	86.67	88.08
Cu	30.72	48.75	7.71	13.59	6.37	7.70	29.99	18.49	57.48	18.15	44.03	17.48	<d.l.< td=""><td>13.50</td><td>6.55</td><td>17.96</td><td></td><td>20.18</td></d.l.<>	13.50	6.55	17.96		20.18
Ni	39.07	89.72	63.07	38.46	51.00	17.05	29.45	42.76	56.86	38.64	71.44	517.48	<d.l.< td=""><td>53.40</td><td>21.16</td><td>74.60</td><td>31.33</td><td>52.73</td></d.l.<>	53.40	21.16	74.60	31.33	52.73
Co	25.43	37.02	24.93	21.00	19.84	23.12	15.12	23.30	19.81	27.12	19.92	21.22	26.53	43.05	32.08	19.06	18.50	18.75
Cr	95.52	317.47	145.40	125.75	90.68	62.15	160.10	129.16	179.72	176.55	310.28	68.22	19.02	119.07	84.00	312.43	54.33	105.08
V	161.66	181.31	161.94	164.17	150.14	173.29	110.25	145.43	118.67	131.67	113.80	54.08	20.39	67.84	65.78	118.10	52.83	55.23
Pb	9.53	5.32	8.93	5.08	8.31	7.73	15.32	7.54	8.73	6.34	9.38	14.32	10.33	14.58	16.65	7.27	19.83	21.55
Th	2.51	2.07	2.27	2.94	2.72	3.07	3.24	4.18	4.53	3.32	4.60	4.33	10.16	8.77	12.20	4.24	6.01	5.19
Ta	0.44	0.23	0.38	0.43	0.40	0.47	0.53	0.42	0.41	0.43	0.36	0.44	0.78	0.66	0.73	0.41	0.73	0.64
U	1.04	0.72	0.81	1.00	0.93	1.05	1.03	1.36	1.53	1.07	1.72	1.08	2.47	3.09	4.01	1.59	2.16	1.44
Mo	2.04	7.39	10.12	5.28	6.89	9.40	5.83	6.41	3.91	10.42	9.21	4.21	0.56	2.24	2.00	7.52	7.81	6.84
Ga	18.16	16.84	17.68	17.12	19.25	18.94	17.81	16.95	16.25	17.79	18.46	20.22	_	-	_	16.72	19.17	18.84
As	3.65	16.89	2.02	2.92	7.69	4.71	2.19	2.41	2.46	7.23	4.28	2.89	-	-	-	4.36	4.27	3.58
Cs	1.56	2.58	2.29	1.99	1.34	0.90	2.35	1600.90	1.69	1.93	1.93	1.38	-	-	-	1.83	0.96	1.81
Mg#	55.86	55.46	54.18	53.24	51.07	50.79	52.68	47.09	47.32	47.22	51.24	50.22	38.25	44.20	52.82	46.52	53.12	49.86
AI	0.45	0.44	0.67	0.49	0.63	0.61	0.60	0.55	0.56	0.59	0.61	0.48	0.86	0.66	0.73	0.70	0.64	0.64
ASI	0.92	0.89	0.76	0.84	0.86	0.89	0.85	0.93	0.90	0.88	0.96	0.87	0.94	0.96	0.98	0.94	0.92	0.94
Sr/Y	68.52	91.26	63.58	49.44	51.25	42.14	50.94	53.76	59.84	64.67	48.23	51.04	9.99	25.61	23.91	37.07	42.72	44.98

^a Samples analyzed in Caltech (USA).

Table 2Chemical composition of the upper lava flows of Guruf volcanics, North Eastern Desert, Egypt.

Rock type	Rhyodacit	e			Rhyolite									
Sample No.	GH1 ^a	GH8 ^a	GH12 ^a	GH18 ^a	Gh4 ^a	GH10 ^a	GH15 ^a	GH39	GH40	GH42	GH45			
SiO ₂	68.63	67.25	69.49	67.56	74.71	74.19	73.68	72.26	71.51	70.75	70.05			
TiO ₂	0.55	0.44	0.46	0.39	0.26	0.19	0.16	0.40	0.42	0.51	0.54			
Al_2O_3	14.18	14.95	15.69	15.02	14.04	11.71	13.06	14.00	14.09	14.71	14.90			
Fe_2O_3	2.87	2.95	3.06	2.64	1.44	2.61	1.57	2.16	2.47	2.55	2.64			
MnO	0.09	0.09	0.09	0.08	0.07	0.01	0.04	0.06	0.06	0.10	0.09			
MgO	0.69	0.76	0.83	0.61	0.18	0.10	0.11	0.28	0.35	0.53	0.49			
CaO	1.56	1.54	1.64	1.77	0.35	0.14	0.70	0.59	0.96	1.35	1.29			
Na ₂ O	6.43	4.64	4.67	4.52	4.72	4.18	3.73	5.48	5.22	5.50	5.78			
K ₂ O	1.81	3.85	3.82	3.89	4.47	3.94	4.66	3.60	3.72	3.50	3.29			
P_2O_5	0.13	0.14	0.14	0.12	0.04	0.01	0.02	0.05	0.07	0.09	0.09			
LOI	0.28	0.76	0.80	0.41	0.38	0.28	0.50	0.71	0.97	0.47	0.46			
Total	97.23	97.36	100.70	97.00	100.66	97.38	98.24	99.59	99.84	100.06	99.62			
Sc	2.08	2.68	2.96	1.77	0.76	2.17	2.44	7.99	7.76	8.23	10.09			
Rb	48.09	97.05	99.40	115.83	88.17	95.06	116.96	68.33	75.53	67.31	78.18			
Ba	928.76	878.17	866.47	826.09	721.07	828.85	693.59	1007.42	1001.49	1032.20	1077.16			
Sr	197.33	310.89	324.41	287.15	57.42	29.75	115.51	121.89	167.02	212.84	261.28			
Nb	14.50	12.22	12.77	12.06	15.08	15.12	14.04	16.94	15.06	16.26	18.27			
Zr	272.64	274.38	254.13	276.27	222.64	272.98	186.51	432.01	366.23	390.06	442.69			
Hf	7.59	7.57	6.93	7.70	7.12	8.11	6.51	11.32	9.70	9.75	11.55			
Y	30.24	26.38	25.02	25.87	32.33	37.06	29.79	40.76	33.89	36.13	42.26			
Zn	46.14	64.99	70.51	59.66	58.11	18.43	44.13	61.92	56.29	63.44	75.44			
Cu	<d.l.< td=""><td><d.l.< td=""><td><d.l.< td=""><td><d.l.< td=""><td><d.l.< td=""><td>3.61</td><td>32.10</td><td>4.99</td><td>5.78</td><td>5.68</td><td>5.76</td></d.l.<></td></d.l.<></td></d.l.<></td></d.l.<></td></d.l.<>	<d.l.< td=""><td><d.l.< td=""><td><d.l.< td=""><td><d.l.< td=""><td>3.61</td><td>32.10</td><td>4.99</td><td>5.78</td><td>5.68</td><td>5.76</td></d.l.<></td></d.l.<></td></d.l.<></td></d.l.<>	<d.l.< td=""><td><d.l.< td=""><td><d.l.< td=""><td>3.61</td><td>32.10</td><td>4.99</td><td>5.78</td><td>5.68</td><td>5.76</td></d.l.<></td></d.l.<></td></d.l.<>	<d.l.< td=""><td><d.l.< td=""><td>3.61</td><td>32.10</td><td>4.99</td><td>5.78</td><td>5.68</td><td>5.76</td></d.l.<></td></d.l.<>	<d.l.< td=""><td>3.61</td><td>32.10</td><td>4.99</td><td>5.78</td><td>5.68</td><td>5.76</td></d.l.<>	3.61	32.10	4.99	5.78	5.68	5.76			
Ni	<d.l.< td=""><td><d.l.< td=""><td>5.99</td><td>2.02</td><td>17.17</td><td><d.l.< td=""><td><d.l.< td=""><td>4.70</td><td>4.89</td><td>5.89</td><td>5.77</td></d.l.<></td></d.l.<></td></d.l.<></td></d.l.<>	<d.l.< td=""><td>5.99</td><td>2.02</td><td>17.17</td><td><d.l.< td=""><td><d.l.< td=""><td>4.70</td><td>4.89</td><td>5.89</td><td>5.77</td></d.l.<></td></d.l.<></td></d.l.<>	5.99	2.02	17.17	<d.l.< td=""><td><d.l.< td=""><td>4.70</td><td>4.89</td><td>5.89</td><td>5.77</td></d.l.<></td></d.l.<>	<d.l.< td=""><td>4.70</td><td>4.89</td><td>5.89</td><td>5.77</td></d.l.<>	4.70	4.89	5.89	5.77			
Co	47.58	22.67	11.02	25.26	35.43	22.24	12.70	0.68	1.76	1.54	2.49			
Cr	32.46	4.57	17.26	17.69	58.11	8.67	5.39	151.46	136.13	190.48	132.43			
V	17.85	27.03	30.65	15.99	6.79	3.84	7.27	15.10	22.90	23.05	23.04			
Pb	5.04	19.02	13.44	20.16	17.06	13.54	22.83	15.65	17.83	15.29	15.67			
Th	7.93	8.15	8.39	9.44	7.27	6.65	8.77	8.98	9.12	7.48	7.78			
Ta	0.71	0.85	0.86	0.89	0.93	0.86	1.07	1.10	1.01	1.02	1.19			
U	2.49	4.15	4.03	4.16	3.92	3.17	4.52	2.78	2.96	2.53	2.54			
Mo	0.65	1.15	1.49	1.53	1.13	0.61	13.32	10.34	9.04	11.24	8.48			
Ga	_	_	_	_	_	_	_	20.58	20.74	18.53	22.89			
As	_	_	_	_	_	_	_	1.13	1.13	2.18	2.81			
Cs	_	_	_	_	_	_	_	0.55	0.53	1.56	1.83			
Mg#	32.30	33.68	34.86	31.47	19.84	7.04	12.51	20.43	21.92	29.17	26.89			
AI	0.88	0.79	0.75	0.78	0.90	0.95	0.86	0.92	0.90	0.87	0.88			
ASI	0.92	1.02	1.06	1.01	1.06	1.03	1.05	1.00	0.98	0.96	0.97			
Sr/Y	6.53	11.79	12.96	11.10	1.78	0.80	3.88	2.99	4.93	5.89	6.18			

^a Samples analyzed in Caltech (USA).

volcanics are dominantly high-K, although some medium-K varieties exist in the lower sequence (Fig. 6c). The analyzed lava flows define a typical calc-alkaline trend on the AFM diagram (Fig. 6d) of Irvine and Baragar (1971).

The new whole-rock major oxide and trace element compositions are shown in variation diagrams in Figs. 7 and 8. The whole suite shows continuous trends with restricted scatter in most elements. With increasing silica, compositions progressively decrease in TiO_2 , Al_2O_3 , Fe_2O_3^* , MgO, CaO and P_2O_5 while increasing in K_2O (Fig. 7). Na $_2\text{O}$ concentrations are scattered and do not correlate well with silica. Rb, Y, Ta, Nb, Hf and Th increase whereas Sr decreases with increasing silica content; Ba is essentially uncorrelated with SiO_2 (Fig. 8).

The alumina saturation index [ASI = A/CNK, where A, C, N, and K are respectively the whole-rock molar abundances of Al_2O_3 , CaO, Na_2O , and K_2O] of the lower lavas are in the metaluminous range, from 0.76 to 0.98 (Table 1), while the upper unit spans the transition to slightly peraluminous, with ASI from 0.92 to 1.06 (Table 2). The agpaitic index (AI = NK/A) of most lava samples is less than 0.87, characteristic of calc-alkaline rocks (Liégeois et al. 1998), except for some more alkaline samples from the rhyolite of upper unit, with 0.92 < AI <1.0. Fractionation of alkali feldspar and quartz do not change AI, but fractionation of plagioclase or other aluminous phases can drive increases in AI towards apparent alkaline character within a single cogenetic suite. On the diagram of Sylvester (1989) for rocks with $SiO_2 > 68$ wt%, the rhyodacite of the upper unit straddles the boundary between the calc-alkaline and alkaline fields, whereas the rhyolite samples lie in the alkaline and highly fractionated

granite fields (Fig. 9a). On the same diagram all the samples of Maurice et al. (2018) with $SiO_2 > 68$ wt% (19 samples) plot in the alkaline field. On the Ga/Al vs. FeO^*/MgO diagram of Whalen et al. (1987), the upper unit rhyolite samples have modestly elevated Ga/Al and plot in the A-type granite field, whereas the other new lava flow analyses plot in the I- and S-type granite field (Fig. 9b). It should be noted that highly fractionated felsic I-type granites can have Ga/Al ratios and some major and trace element values that overlap those of typical A-type granites (Whalen et al. 1987).

Most of the lava flows (basaltic andesite, andesite and dacite) of the lower succession have low Y and Yb contents and high (Sr/Y) and (La/Yb)_n ratios. Based on the geochemical definition of "adakite" proposed by Defant and Drummond (1990), these Guruf samples have modestly to moderately adakitic character (Fig. 9c, d). The more primitive whole-rock analyses of Maurice et al. (2018) likewise extend into the adakitic field. Similar adakitic volcanic suites have been noted in many localities in the ANS, where they are strongly associated with post-collisional calc-alkaline activity (Abdelfadil et al. 2018; Be'eri-Shlevin et al. 2011; Eliwa et al. 2006; Obeid and Azer 2015).

Primitive mantle-normalized trace-element concentrations of the lava samples define a series of related, nearly parallel, patterns with continuous enrichment in most elements from basaltic andesite through andesite to rhyolite, coupled with deepening negative anomalies in Sr, P, and Ti (Fig. 10a). The data of Maurice et al. (2018) are similar. All the lavas are enriched in large ion lithophile elements (LILE) relative to high field strength elements (HFSE), expressed by troughs in the patterns at Ta and Nb relative to Th and Ce.

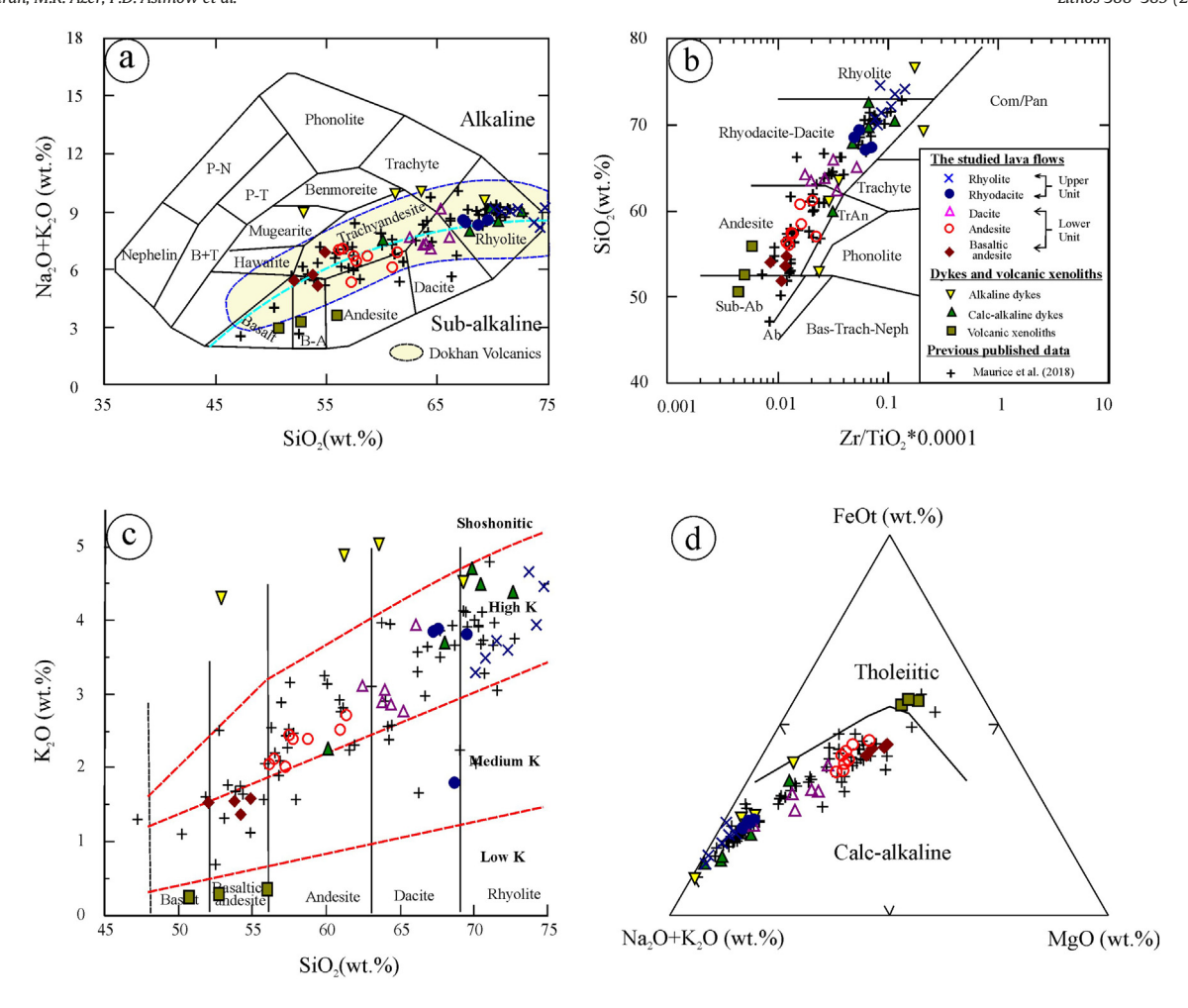


Fig. 6. Whole-rock chemical classification diagrams: (a) total alkalis vs. silica (TAS) diagram (Cox et al. 1979); the field of Dokhan volcanics is adopted from Azer and Farahat (2011); (b) SiO₂ versus Zr/TiO₂ diagram (after Winchester and Floyd 1977); (c) SiO₂ versus K₂O diagram (after Rickwood 1989); (d) AFM diagram (after Irvine and Baragar 1971).

Concentrations of rare earth elements (REE) and key ratios of REE concentrations are given in Tables 3 and 4. Chondrite-normalized REE patterns are presented in Figure 10b. Data given by Maurice et al. (2018) overlap the new results for the most part; the inclusion of rhyolitic ignimbrite extends to greater REE enrichment than any of the new lava samples and the Maurice et al. data includes one dacite with anomalously low LREE. The Guruf volcanic rocks are enriched in LREE relative to HREE [(La/Yb)_n = 5.6–14.5). The basaltic andesite samples have slightly concave-upwards HREE patterns, which evolve to flat HREE profiles in the other lava types. Eu concentrations relative to neighboring REE decrease through the volcanic suite, from positive anomalies [Eu/Eu* = 1.07–1.33] in basaltic andesite, to slightly negative or small positive anomalies [Eu/Eu* = 0.98–1.21] in andesite, consistently negative anomalies [Eu/Eu* = 0.71–0.96] in dacite and rhyodacite, and pronounced negative anomalies [Eu/Eu* = 0.35–0.73] in rhyolite.

6.1.2. Dikes and volcanic xenoliths

Major and trace element analyses of 10 dike samples and 3 samples of metavolcanic xenoliths in granodiorite (Table 5) are presented to constrain their relationship to the Guruf volcanics. The dikes vary widely in composition (53.0–76.7 wt% SiO₂). The older dikes include trachyandesite and rhyolite, while the strongly alkaline younger dikes include mugearite, benmoreite, trachyte and rhyolite (Fig. 6a). The calc-alkaline dikes belong to the high-K series, whereas the alkaline dikes are shoshonitic (Fig. 6c). The calc-alkaline dikes resemble the Guruf volcanics in major elements (Fig. 6a–d), whereas the alkaline dikes are plainly distinct. The metavolcanic xenoliths are all relatively

primitive (50.8–56.0 wt% SiO₂) basalt, basaltic andesite, or andesite (Fig. 6a, b). They plainly belong to the tholeiitic low-K series (Fig. 6c, d). They resemble the island-arc metavolcanic sequences of the ANS (Shadli metavolcanics; Abdel-Karim et al. 2019) and are compositionally unrelated to the Dokhan volcanics (contrary to Basta et al. 2017). Although some of the most primitive volcanic analyses of Maurice et al. (2018) resemble the metavolcanic xenolith compositions in selected plots, they do not overlap in other plots (e.g., Fig. 6b, c) and their trace element character is totally different.

The primitive mantle-normalized trace element (Fig. 11a) and chondrite-normalized REE (Fig. 11b) patterns of the calc-alkaline dikes are fully encompassed by the range of Guruf volcanic data, whereas the patterns of the alkaline dikes and metavolcanic xenoliths are plainly different. The alkaline dikes are highly enriched in \sum REE, while the metavolcanic xenoliths have unfractionated REE and much lower LREE and LILE concentrations than any Guruf volcanic sample (Fig. 11b, Table 6). The REE patterns of the metavolcanic xenoliths are similar to those of the Shadli metavolcanics (Abdel-Karim et al. 2019).

6.2. Tectonic setting

The present and previous studies confirm that the Guruf volcanic suite is a member of the larger calc-alkaline Dokhan volcanic assemblage. Hence this work can contribute to resolving the long-running discrepancy in the literature regarding the tectonic setting of this volcanic phase, which has been variously assigned to a subduction environment (Abdel Rahman, 1996; Maurice et al. 2018), an extensional setting that

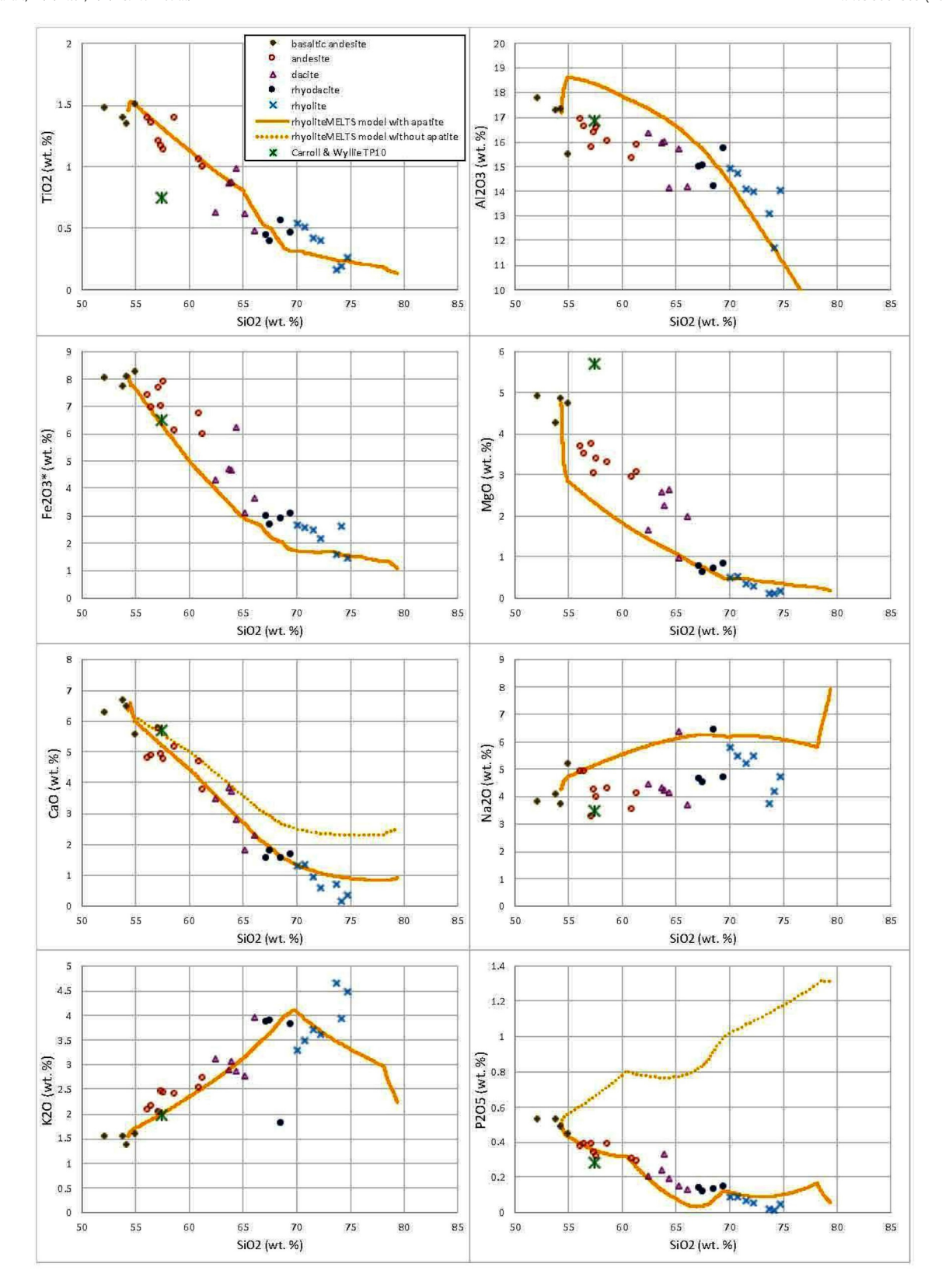


Fig. 7. Silica variation diagrams of some major oxides. Model curves, discussed in section 7.4 of the text, are shown as well. The dashed curves in the CaO and P_2O_5 panels show the predictions of rhyoliteMELTS 1.0.2 for fractional crystallization along a linear pressure-temperature path from the liquidus at 1155 °C and 300 MPa to 722 °C at 125 MPa, with 2.0 wt% initial H_2O and along the NNO oxygen buffer. The solid curves show a modified model in which 0.0004 wt% apatite is fractionated for each 1 °C of cooling.

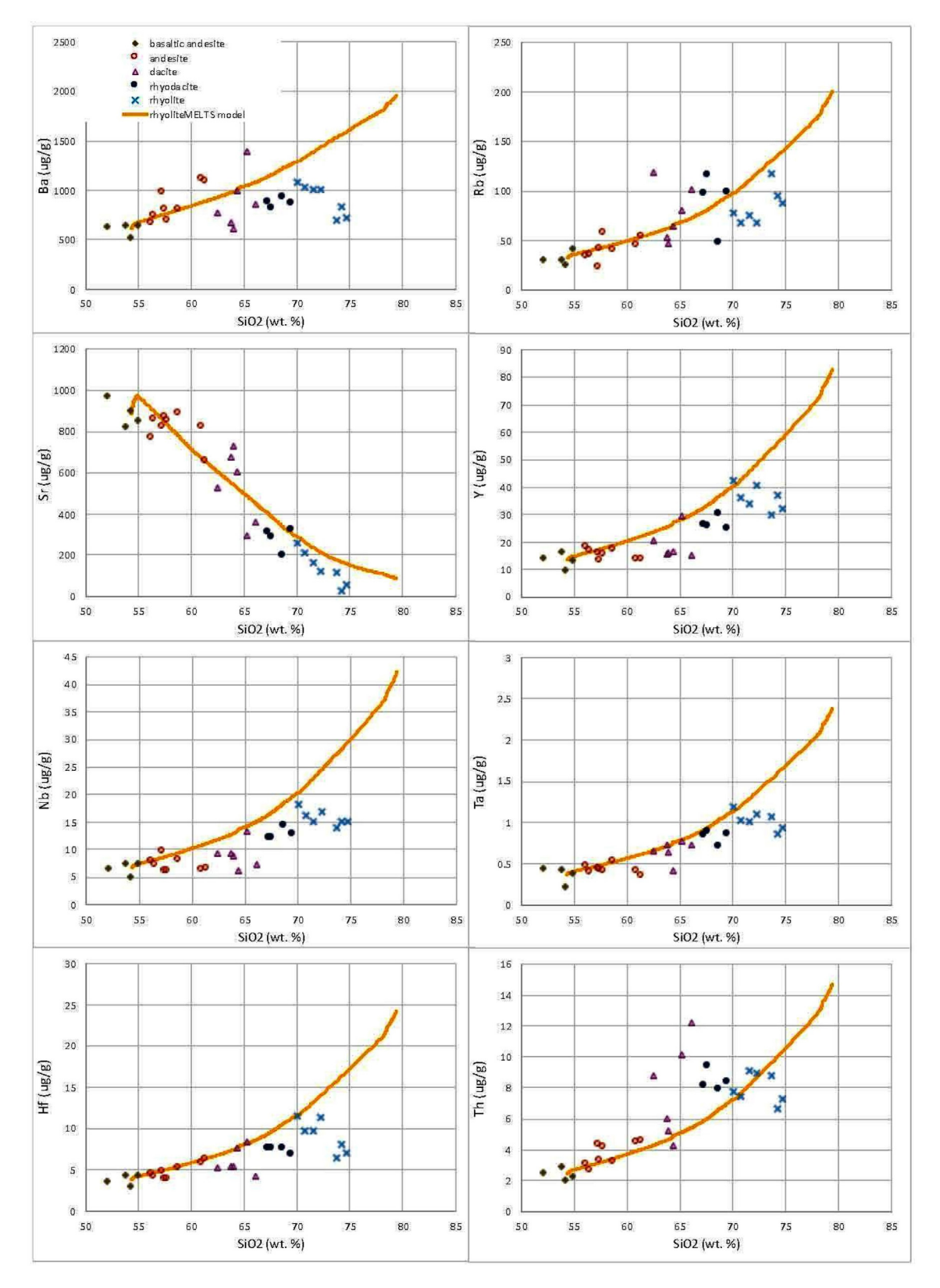


Fig. 8. Silica variation diagrams of some trace elements. Symbols as in Fig. 7. Model curves are discussed in section 7.4.

post-dates crustal thickening (Mohammed et al., 2000; Abu El-Enen et al. 2018), or a post-collisional transition from subduction to extension (Ressetar and Monard, 1983; Eliwa et al. 2006, 2014; Azer and Farahat 2011; Obeid and Azer 2015).

One source of controversy about the tectonic assignment of the Dokhan volcanics is the geochemical overlap in many cases between subduction-related and post-collisional magmatism. Although Pearce et al. (1984) proposed a volcanic discrimination diagram, Rb vs.

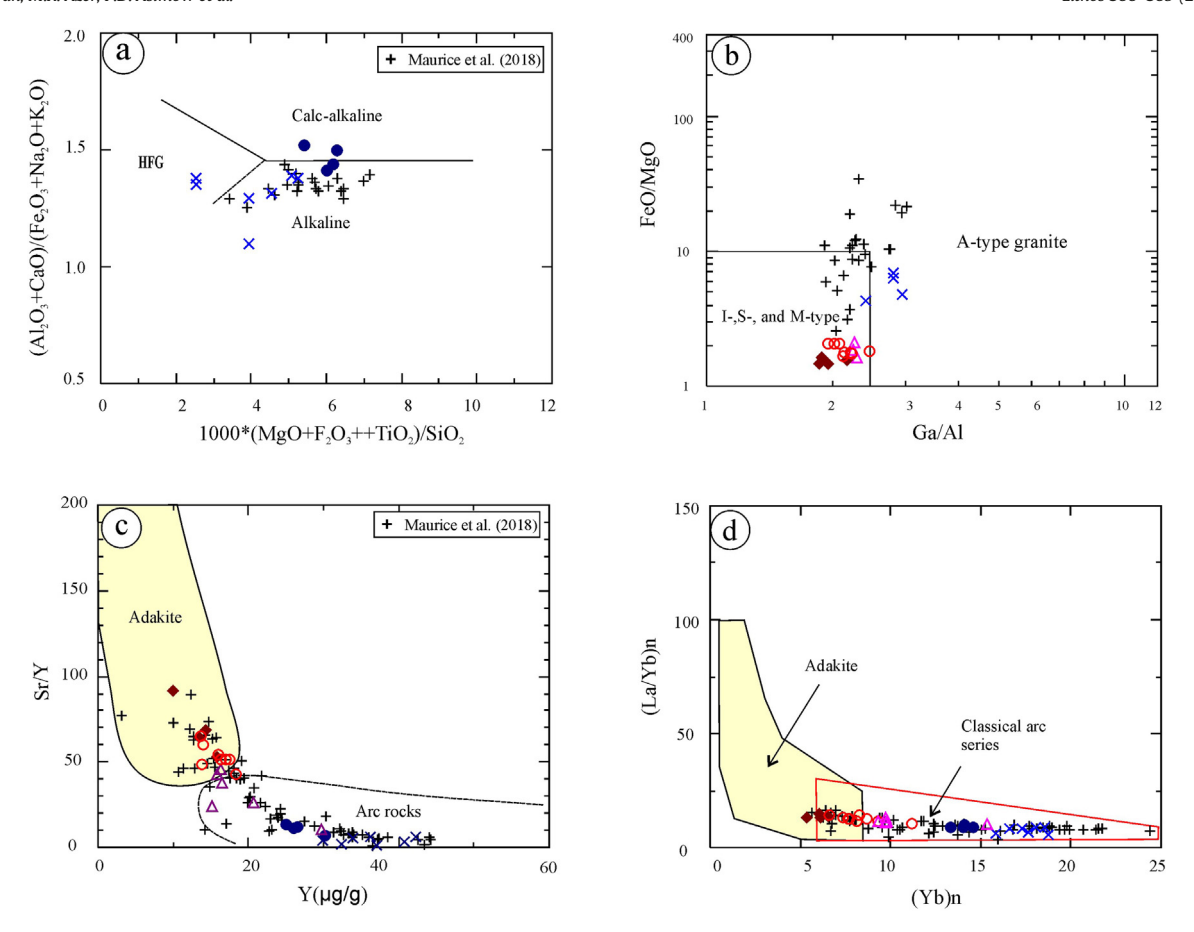


Fig. 9. More whole-rock discrimination diagrams: (a) 100* (MgO + Fe₂O₃ + TiO₂)/SiO₂ vs. (Al₂O₃ + CaO)/(Fe₂O₃ + Na₂O + K₂O) (after Sylvester, 1989); (b) Ga/Al vs. FeO*/MgO (after Whalen et al. 1987), (c) Y vs. Sr/Y (after Defant and Drummond 1990), and (d) (Yb)_n vs (La/Yb)_n classification diagram (after Defant and Drummond 1990). Symbols as in Fig. 6.

Y + Nb, that separates volcanic-arc granite (VAG) from within-plate granite (WPG), Pearce (1996) later added a post-collisional granite field that fully overlaps the boundary between VAG and WPG. In the Guruf case, the metavolcanic xenoliths plot exclusively in the VAG region, the lower unit of Guruf volcanics crosses from the upper part of the VAG field into the area of post-collisional granites, and the upper unit rhyolites plot within the post-collisional field at the boundary separating VAG from WPG (Fig. 12a). The SiO₂-Nb discrimination diagram of Pearce and Gale (1977) also provides no clear decision about the Guruf suite; again, the metavolcanic xenoliths plot as clearly arcrelated but the volcanic samples straddle the boundary between the volcanic arc field and the area of overlap between orogenic and anorogenic rocks (Fig. 12b). On the Rb-Hf-Ta diagram of Harris et al. (1986), the Guruf volcanics plot in the volcanic arc field but lie close to the boundary of the within-plate field (Fig. 12c). As noted above, samples with $SiO_2 > 68$ wt% in the present study and in Maurice et al. (2018) have high AI (>0.87) and plot in Sylvester's (1989) alkaline field (Fig. 9a). These features are not observed in subduction-related volcanic sequences in the ANS; they are characteristic instead of the post-collisional calc-alkaline volcanic units (Be'eri-Shlevin et al. 2011).

Authors that have adopted a subduction-related tectonic setting for the Dokhan volcanics exposed around G. Um Guruf have reasoned mainly from their chemical compositions, which are indeed in many regards similar to those of typical Andean calc-alkaline volcanic rocks (Maurice et al. 2018). However, the high-K calc-alkaline character and other traits previously interpreted to indicate arc magmatism for the Dokhan volcanics may simply reflect remelting of arc material or enriched lithospheric mantle from the earlier subduction period of ANS evolution. Similar inheritance is observed in post-collisional plutonic rocks in the ANS (Azer et al. 2012; Gahlan et al. 2016) and

elsewhere around the world. Consequently, the persistence of a subduction signature in some potential magmatic source region from the end of island arc activity until the early phase of Dokhan volcanism seems reasonable. This is supported by the lull in magmatic activity (740-640 Ma) between the end of the subduction-related island-arc stage and the beginning of post-collisional volcanic activity in most of the northernmost ANS (Samuel et al. 2011), although ages spanning this gap have been reported from the southern ANS (Ali et al. 2010; Johnson and Kattan 2007). Field relations plainly show that the Guruf volcanics are younger than the subjacent, subduction-related calcalkaline quartz-diorite and granodiorite (Moghazi et al. 2004) and older than the voluminous within-plate alkali feldspar granites. The use of metavolcanic xenoliths in the granodiorite to suggest that the pluton postdates the Dokhan volcanics (Basta et al. 2017) turns out to be incorrect; these xenoliths plot completely in the volcanic arc field are not related to even the most primitive of the Dokhan lavas. Indeed, enough time passed after emplacement of the subduction-related plutonic rocks for them to be unroofed, exposed, and covered unconformably by surface lava flows of the Guruf series.

Maurice et al. (2018) argued that the ages of younger Dokhan felsic rocks (Abu El-Enen et al. 2018; Breitkreuz et al. 2010) do not support dividing the Dokhan volcanic rocks in the North Eastern Desert into two successive but related cycles. They focus on a 5 m.y. gap between the youngest dated members of the lower cycle and the oldest dated member of the upper cycle as evidence that the cycles are unrelated. Instead, they group the lower cycle with a tectonic setting that is thought to have ended tens of m.y. earlier. Thus, they propose to restrict use of the term "Dokhan volcanics" to the calc-alkaline andesitic to dacitic volcanic rocks, excluding the later rhyolites. Their conclusion that there was persistent subduction at this location until the time of emplacement of the

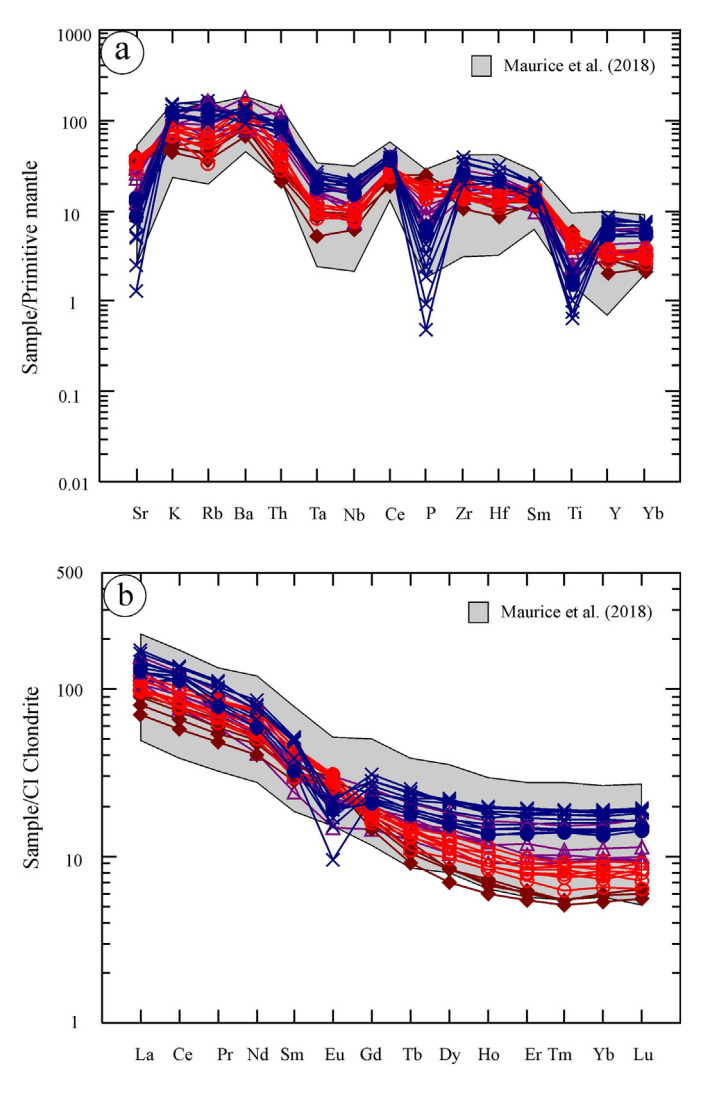


Fig. 10. Normalized trace-element diagrams for lava flow: (a) primitive-mantle normalized extended trace element patterns and (b) CI-Chondrite normalized REE plots. Primitive mantle and CI-Chondrite normalization values are from Pearce (1983) and Sun and McDonough (1989), respectively. Symbols as in Fig. 6. (c) Results of the rhyoliteMELTS fractionation model for REE patterns. The dashed lines show the nominal model results, whereas the solid lines show the result of added apatite fractionation.

Dokhan volcanics is then based only on the lower unit samples. This is contrary to the general consensus among Egyptian scientists studying the Dokhan volcanics since 1934 that the sequence can be subdivided into upper and lower units, with the upper one consisting essentially of rhyolite (Abdelfadil et al. 2018; El-Gaby et al. 1991; Obeid and Azer 2015). Moreover, rhyolite is present in the lower Dokhan volcanic series (Be'eri-Shlevin et al. 2011). Rhyolite with A-type character is observed in many of the calc-alkaline Dokhan volcanic exposures in the Eastern Desert and Sinai, especially in the upper unit (Be'eri-Shlevin et al. 2011).

The data of Maurice et al. (2018) extend from the island arc field into the continental margin arc field in several trace element ratio diagrams (their Fig. 13), which they attributed to temporal variation in island arc crust thickness over the lifetime of Dokhan volcanic activity, dismissing on isotopic grounds the possibility of a continental margin (Andean type) arc setting. However, the references invoked to support the absence of old continental crust in the Eastern Desert and the low initial ⁸⁷Sr/⁸⁶Sr ratios of the Dokhan volcanic rocks (Ali et al. 2012; Liégeois and Stern 2010) are incomplete. Other authors report abundant isotopic evidence for involvement of old continental crust underlying the juvenile crust of the northern ANS (e.g., Be'eri-Shlevin et al. 2011; Hargrove et al. 2006; Li et al. 2018; Samuel et al. 2011; Wilde and Youssef 2002). Moreover, the arc crust thickness at the end of the lower Dokhan cycle inferred by Maurice et al. (2018) using the (La/

Yb)_n proxy, 50 km, is significantly greater than the modern depth to the seismic Moho in the ANS (23–39 km; Al-Damegh et al. 2005). It is likely that the depletion of Yb due to the adakitic character of the lower Dokhan sequence in the area (Abdelfadil et al. 2018; Be'eri-Shlevin et al. 2011; Eliwa et al. 2006; Obeid and Azer 2015) leads to an exaggerated estimate of crustal thickness. Finally, Maurice et al. (2018) applied some coarse tectonic discrimination diagrams based on the chemistry of clinopyroxene (Leterrier et al. 1982) that are not adequate for distinguishing active subduction island arc activity from post-collisional continental margin activity.

High-precision U—Pb dating for subduction-related volcanic rocks in the Eastern Desert shows that their ages range from 720 Ma to 770 Ma (Ali et al. 2010). Recent U—Pb dating of the post-collisional phase in the ANS includes both plutonic rocks and their volcanic equivalents and ranges between 630 and 590 Ma (Be'eri-Shlevin et al. 2011; Moussa et al. 2008). U—Pb zircon dating of the Dokhan Volcanics indicates that the early pulse began at 630 Ma, whereas the later pulse ended around 590 Ma (Abu El-Enen et al. 2018; Be'eri-Shlevin et al. 2011; Breitkreuz et al. 2010; Wilde and Youssef 2000). Many authors have emphasized that there is no evidence for subduction or collisional related processes in the ANS later than ~635–620 Ma (e.g., Avigad and Gvirtzman 2009; Eyal et al. 2010), which suggests that the Dokhan volcanics post-date the subduction period. Therefore, there is a general

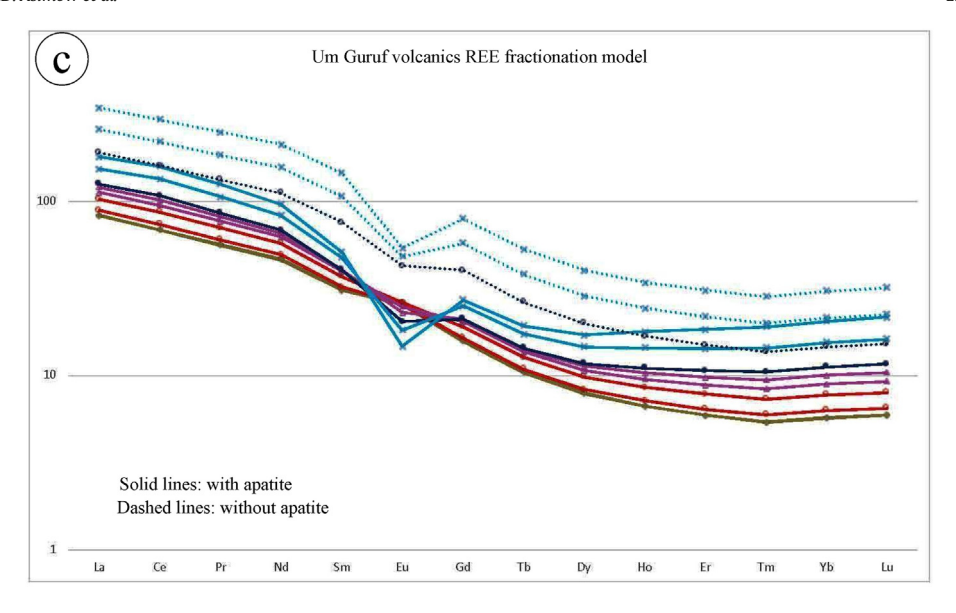


Fig. 10 (continued).

consensus that the Dokhan volcanics formed in a post-collisional tectonic setting (Be'eri-Shlevin et al. 2011; Azer and Farahat 2011, and many others). Also, the two pulses of volcanic activity in the Dokhan volcanics are comparable with the two magmatic phases of post-collisional plutonic activity: an early magmatic phase at ca. 635–620 Ma and a later one at 610–590 Ma (Be'eri-Shlevin et al. 2011; Eyal et al. 2010). All these criteria support a post-collisional setting for the studied volcanics rather than an active subduction setting.

7. Discussion

7.1. Petrogenesis

The Guruf volcanics include intermediate to silicic volcanics and lack basalts, a feature common to sequences assigned to the Dokhan volcanic series in the Eastern Desert; all the Guruf samples plot within the Dokhan field in the TAS diagram (Fig. 6a). The handful of basalts recorded by Maurice et al. (2018) are puzzling; some of them plot outside

the field of Dokhan volcanics (Fig. 6a). Possibly they represent a lower stratigraphic unit unrelated to the Guruf volcanics; not enough field context is presented to be sure. In any case, they are highly altered; their low apparent SiO₂ is the result of their high LOI. The intermediate and silicic magmas of the Guruf successions display continuous trends without any compositional gaps (Figs. 7, 8), suggesting a common source. Also, they have closely related and progressively evolving trace elements and REE patterns (Fig. 10a, b).

Maurice et al. (2018) distinguished the Dokhan volcanic rocks of the W. Hamad area, including the Guruf volcanics, into an early pulse dominated by basalt and andesite and a later pulse dominated by dacite. On the basis of the basaltic samples, Maurice et al. (2018) judged that the primary magmas of the entire sequence must be mantle-derived and described it as unlikely that subduction-influenced mantle asthenosphere could persist beneath the ANS for tens of m.y. beyond the end of subduction. The evolving trace element character of the suite was taken to indicate an evolution in arc maturity. However, as the earlier island arc stage in the Eastern Desert of Egypt evolved from immature to

Table 3REE concentrations of the lower lava flows of Guruf volcanics, North Eastern Desert, Egypt.

Rock type	Basaltic	andesite	;		Andesit	te							Dacite					
Sample	GH22	GH23	GH26	GH27	GH28	GH30	GH31	GH32	GH33	GH34	GH35	GH36	GH2 ^a	GH3 ^a	GH13 ^a	GH24	GH25	GH29
La	16.72	19.26	21.28	21.89	22.94	22.54	26.63	26.42	28.29	23.94	23.32	24.20	37.34	29.26	26.20	25.70	27.73	30.77
Ce	35.46	40.49	45.04	47.77	53.20	46.99	59.10	58.90	62.43	52.20	51.56	47.94	77.47	57.21	47.54	56.86	54.64	55.73
Pr	4.59	5.15	5.57	6.21	6.98	6.04	7.92	7.89	8.10	6.76	6.44	6.04	9.16	7.05	5.58	7.25	6.61	7.21
Nd	18.81	21.89	22.91	24.16	31.11	25.11	34.19	34.09	34.79	29.66	26.49	23.62	34.98	25.77	19.46	28.56	25.06	27.70
Sm	4.31	4.81	4.85	5.34	6.64	4.93	6.97	6.95	6.87	6.27	4.94	4.57	6.03	4.58	3.67	6.31	5.82	5.34
Eu	1.56	1.46	1.43	1.71	1.70	1.61	1.77	1.65	1.80	1.69	1.54	1.49	1.77	1.29	0.86	1.49	1.36	1.26
Gd	2.97	3.29	3.46	3.64	3.56	3.37	4.13	3.83	3.94	3.72	3.74	3.29	5.22	4.09	2.95	4.18	3.98	3.85
Tb	0.34	0.39	0.42	0.45	0.50	0.41	0.56	0.52	0.53	0.53	0.56	0.49	0.77	0.59	0.46	0.58	0.64	0.59
Dy	1.76	2.10	2.18	2.11	2.65	2.48	3.34	3.14	2.94	2.82	2.91	2.80	4.58	3.43	2.65	3.34	3.45	3.65
Но	0.34	0.39	0.38	0.41	0.49	0.47	0.64	0.59	0.54	0.49	0.59	0.49	0.91	0.66	0.52	0.68	0.69	0.69
Er	0.91	0.99	1.00	1.03	1.31	1.18	1.61	1.50	1.40	1.29	1.39	1.31	2.64	1.95	1.51	1.67	1.67	1.70
Tm	0.13	0.14	0.14	0.14	0.20	0.16	0.23	0.22	0.22	0.20	0.21	0.19	0.39	0.28	0.23	0.26	0.24	0.23
Yb	0.90	0.98	0.99	1.02	1.37	1.11	1.58	1.47	1.40	1.25	1.29	1.31	2.61	1.90	1.58	1.65	1.66	1.65
Lu	0.14	0.15	0.15	0.16	0.20	0.16	0.23	0.21	0.23	0.20	0.21	0.18	0.42	0.29	0.24	0.25	0.24	0.23
Eu/Eu*	1.33	1.12	1.07	1.19	1.07	1.21	1.01	0.98	1.06	1.07	1.10	1.17	0.96	0.91	0.80	0.89	0.86	0.85
$(La/Yb)_n$	12.56	13.29	14.54	14.51	11.34	13.77	11.43	12.18	13.71	12.94	12.25	12.45	9.67	10.44	11.18	10.55	11.32	12.63
$(La/Sm)_n$	2.45	2.53	2.77	2.59	2.18	2.89	2.41	2.40	2.60	2.41	2.98	3.34	3.91	4.03	4.51	2.57	3.01	3.64
(Gd/Lu) _n	2.60	2.69	2.83	2.79	2.21	2.55	2.25	2.27	2.15	2.30	2.21	2.24	1.54	1.72	1.52	2.03	2.01	2.02
(La/Lu) _n	12.24	13.16	14.54	14.02	11.87	14.26	12.13	13.08	12.88	12.39	11.54	13.78	9.19	10.32	11.26	10.45	11.69	13.47

^a Samples analyzed in Caltech (USA).

 Table 4

 REE concentrations of the upper lava flows of Guruf volcanics, North Eastern Desert, Egypt.

Rock type	Rhyodacit	e	·		Rhyolite								
Sample No.	GH1 ^a	GH8 ^a	GH12 ^a	GH18 ^a	Gh4 ^a	GH10 ^a	GH15 ^a	GH39	GH40	GH42	GH45		
La	34.28	30.21	30.08	31.83	29.66	26.39	25.21	38.52	34.95	35.09	40.75		
Ce	75.32	69.18	68.29	74.80	73.56	68.68	72.57	82.35	74.40	75.63	84.18		
Pr	8.34	7.50	7.40	7.89	7.97	7.13	6.67	10.41	9.48	9.67	10.67		
Nd	32.10	27.62	27.81	28.71	30.58	27.24	25.05	37.20	35.36	39.89	37.12		
Sm	5.67	4.90	5.17	5.58	5.86	5.22	5.11	7.75	7.43	7.90	7.49		
Eu	1.62	1.11	1.13	1.16	0.88	0.88	0.55	1.09	0.99	1.24	1.27		
Gd	4.87	4.28	4.39	4.47	5.02	4.99	4.55	5.85	5.40	6.29	5.79		
Tb	0.71	0.66	0.66	0.69	0.79	0.81	0.72	0.89	0.82	0.95	0.91		
Dy	4.32	3.95	3.86	4.05	4.72	5.21	4.25	5.39	5.59	5.26	5.49		
Но	0.83	0.77	0.75	0.82	0.96	1.06	0.88	1.09	1.05	1.03	1.13		
Er	2.38	2.25	2.30	2.45	2.96	3.03	2.58	3.12	2.97	2.82	3.18		
Tm	0.36	0.35	0.35	0.37	0.45	0.47	0.40	0.47	0.45	0.42	0.48		
Yb	2.40	2.38	2.27	2.48	3.00	3.19	2.69	3.08	2.94	2.82	3.16		
Lu	0.37	0.38	0.36	0.38	0.49	0.49	0.42	0.47	0.46	0.41	0.48		
Eu/Eu*	0.94	0.74	0.73	0.71	0.50	0.52	0.35	0.49	0.48	0.54	0.59		
(La/Yb) _n	9.67	8.60	8.94	8.68	6.68	5.59	6.35	8.46	8.04	8.41	8.72		
(La/Sm) _n	3.82	3.89	3.67	3.60	3.20	3.19	3.12	3.14	2.97	2.80	3.43		
(Gd/Lu) _n	1.60	1.39	1.50	1.45	1.27	1.26	1.34	1.53	1.44	1.88	1.48		
(La/Lu) _n	9.40	8.19	8.58	8.62	6.26	5.55	6.21	8.40	7.78	8.77	8.70		

^a Samples analyzed in Caltech (USA).

 Table 5

 Chemical composition of the dykes and volcanic xenoliths associated with Guruf volcanics, North Eastern Desert, Egypt.

Rock type	Dykes	Dykes											
	Alkaline dy	ykes				Calc-alka	line dykes						
Sample No.	GH9 ^a	GH14 ^a	Gh20 ^a	GH11 ^a	GH19 ^a	GH7 ^a	Gh17 ^a	Gh5 ^a	GH16 ^a	GH6 ^a	Xen.1	Xen.6	Xen.9
SiO ₂	61.26	52.99	63.62	76.73	69.33	72.65	60.13	69.87	70.51	68.02	56.02	50.78	52.81
TiO ₂	0.95	1.92	0.82	0.12	0.32	0.35	0.94	0.33	0.21	0.41	1.03	1.18	1.12
Al_2O_3	17.18	17.80	17.02	11.92	11.67	14.11	16.75	14.36	13.71	14.54	16.06	16.14	16.09
Fe_2O_3	4.29	7.73	3.75	1.00	3.86	1.93	5.35	1.82	1.51	2.65	11.31	12.24	12.11
MnO	0.13	0.10	0.12	0.03	0.09	0.07	0.09	0.05	0.07	0.07	0.21	0.28	0.25
MgO	0.86	1.35	0.76	0.04	0.42	0.44	1.28	0.47	0.06	0.84	4.59	5.54	4.98
CaO	2.69	4.72	2.35	0.26	0.41	0.71	4.10	0.82	1.28	1.70	4.93	8.48	6.17
Na ₂ O	5.05	4.68	4.99	4.01	5.10	4.63	5.30	4.48	4.01	4.29	3.26	2.71	3.01
K ₂ O	4.91	4.32	5.05	4.21	4.53	4.41	2.28	4.72	4.51	3.73	0.36	0.27	0.31
P_2O_5	0.39	1.04	0.29	0.01	0.03	0.08	0.31	0.08	0.03	0.12	0.19	0.27	0.21
LOI	0.30	0.91	0.31	0.45	0.52	0.43	1.08	0.82	1.49	0.92	1.63	2.06	1.97
Total	98.01	97.55	99.07	98.77	96.27	99.80	97.63	97.80	97.40	97.29	99.59	99.95	99.03
Sc	0.96	3.04	1.23	1.84	0.74	0.91	2.81	1.76	1.61	1.80	39.40	42.70	41.30
Rb	51.29	98.42	61.02	231.56	118.17	116.51	51.30	156.68	134.95	88.60	10.10	4.40	6.20
Ba	3140.09	1896.32	2467.76	232.41	225.94	744.66	665.15	831.32	965.00	808.78	166.60	107.30	125.80
Sr	443.92	1648.45	361.44	89.88	29.78	175.88	651.23	237.80	115.04	390.88	281.40	176.50	211.10
Nb	20.95	22.12	22.74	48.77	102.87	12.13	10.60	11.12	13.07	8.73	3.80	2.40	3.20
Zr	272.19	449.70	294.43	207.20	657.47	228.57	296.04	215.90	240.17	195.74	60.30	52.50	56.40
Hf	5.89	7.63	6.61	10.01	17.93	6.56	7.33	5.99	7.18	5.49	2.20	1.70	2.10
Y	30.45	27.96	32.03	58.79	81.44	22.11	24.81	20.58	26.85	15.28	29.60	24.10	25.40
Zn	81.92	84.48	84.44	49.45	141.54	37.31	80.17	31.85	29.96	110.93	72.40	86.40	77.40
Cu	<d.l.< td=""><td>3.40</td><td><d.l.< td=""><td><d.l.< td=""><td><d.l.< td=""><td><d.l.< td=""><td><d.l.< td=""><td><d.l.< td=""><td>1.52</td><td><d.l.< td=""><td>399.50</td><td>99.40</td><td>84.00</td></d.l.<></td></d.l.<></td></d.l.<></td></d.l.<></td></d.l.<></td></d.l.<></td></d.l.<></td></d.l.<>	3.40	<d.l.< td=""><td><d.l.< td=""><td><d.l.< td=""><td><d.l.< td=""><td><d.l.< td=""><td><d.l.< td=""><td>1.52</td><td><d.l.< td=""><td>399.50</td><td>99.40</td><td>84.00</td></d.l.<></td></d.l.<></td></d.l.<></td></d.l.<></td></d.l.<></td></d.l.<></td></d.l.<>	<d.l.< td=""><td><d.l.< td=""><td><d.l.< td=""><td><d.l.< td=""><td><d.l.< td=""><td>1.52</td><td><d.l.< td=""><td>399.50</td><td>99.40</td><td>84.00</td></d.l.<></td></d.l.<></td></d.l.<></td></d.l.<></td></d.l.<></td></d.l.<>	<d.l.< td=""><td><d.l.< td=""><td><d.l.< td=""><td><d.l.< td=""><td>1.52</td><td><d.l.< td=""><td>399.50</td><td>99.40</td><td>84.00</td></d.l.<></td></d.l.<></td></d.l.<></td></d.l.<></td></d.l.<>	<d.l.< td=""><td><d.l.< td=""><td><d.l.< td=""><td>1.52</td><td><d.l.< td=""><td>399.50</td><td>99.40</td><td>84.00</td></d.l.<></td></d.l.<></td></d.l.<></td></d.l.<>	<d.l.< td=""><td><d.l.< td=""><td>1.52</td><td><d.l.< td=""><td>399.50</td><td>99.40</td><td>84.00</td></d.l.<></td></d.l.<></td></d.l.<>	<d.l.< td=""><td>1.52</td><td><d.l.< td=""><td>399.50</td><td>99.40</td><td>84.00</td></d.l.<></td></d.l.<>	1.52	<d.l.< td=""><td>399.50</td><td>99.40</td><td>84.00</td></d.l.<>	399.50	99.40	84.00
Ni	<d.l.< td=""><td>23.34</td><td><d.l.< td=""><td>1.89</td><td>21.21</td><td>56.82</td><td>7.24</td><td>4.48</td><td><d.l.< td=""><td>3.32</td><td>19.40</td><td>22.50</td><td>20.50</td></d.l.<></td></d.l.<></td></d.l.<>	23.34	<d.l.< td=""><td>1.89</td><td>21.21</td><td>56.82</td><td>7.24</td><td>4.48</td><td><d.l.< td=""><td>3.32</td><td>19.40</td><td>22.50</td><td>20.50</td></d.l.<></td></d.l.<>	1.89	21.21	56.82	7.24	4.48	<d.l.< td=""><td>3.32</td><td>19.40</td><td>22.50</td><td>20.50</td></d.l.<>	3.32	19.40	22.50	20.50
Co	23.31	34.14	28.00	27.95	2.37	22.41	61.78	33.19	20.27	50.17	42.20	55.30	44.20
Cr	8.74	15.48	19.04	16.67	46.00	121.58	34.36	30.88	10.06	36.37	14.60	50.20	29.60
V	22.60	141.87	16.04	4.76	15.86	21.37	58.94	17.27	<d.l.< td=""><td>38.87</td><td>338.90</td><td>372.10</td><td>363.70</td></d.l.<>	38.87	338.90	372.10	363.70
Pb	13.54	34.10	13.86	14.92	7.68	7.39	20.61	5.16	42.02	113.74	14.70	13.80	10.20
Th	4.18	3.32	5.65	36.44	5.56	11.87	7.39	10.24	6.70	10.82	0.90	1.70	1.20
Ta	1.00	1.57	1.12	3.43	6.42	0.88	0.55	0.82	0.91	0.90	0.20	0.10	0.20
U	2.00	1.56	2.45	7.88	3.25	4.18	2.22	4.33	4.81	4.61	0.40	0.30	0.20
Mo	1.51	1.16	2.17	0.54	1.36	1.89	1.24	1.27	1.74	3.78	1.80	1.40	1.50
Ga	_	_	_	_	_	_	_	_	_	_	14.20	11.70	13.60
As	_	_	_	_	_	_	_	_	_	_	0.86	0.93	1.01
Cs	_	_	_	_	_	_	_	_	_	_	0.48	0.52	0.64
Mg#	28.46	25.69	28.64	7.68	17.68	31.17	32.17	33.97	7.84	38.61	44.57	47.28	44.89
AI	0.79	0.70	0.80	0.94	1.14	0.88	0.67	0.87	0.84	0.76	0.36	0.29	0.33
ASI	0.73	0.75	0.95	1.03	0.83	1.03	0.90	1.03	0.99	1.02	1.09	0.80	0.97
Sr/Y	14.58	58.96	11.28	1.53	0.83	7.95	26.25	11.56	4.29	25.59	9.51	7.32	8.31

^a Samples analyzed in Caltech (USA).

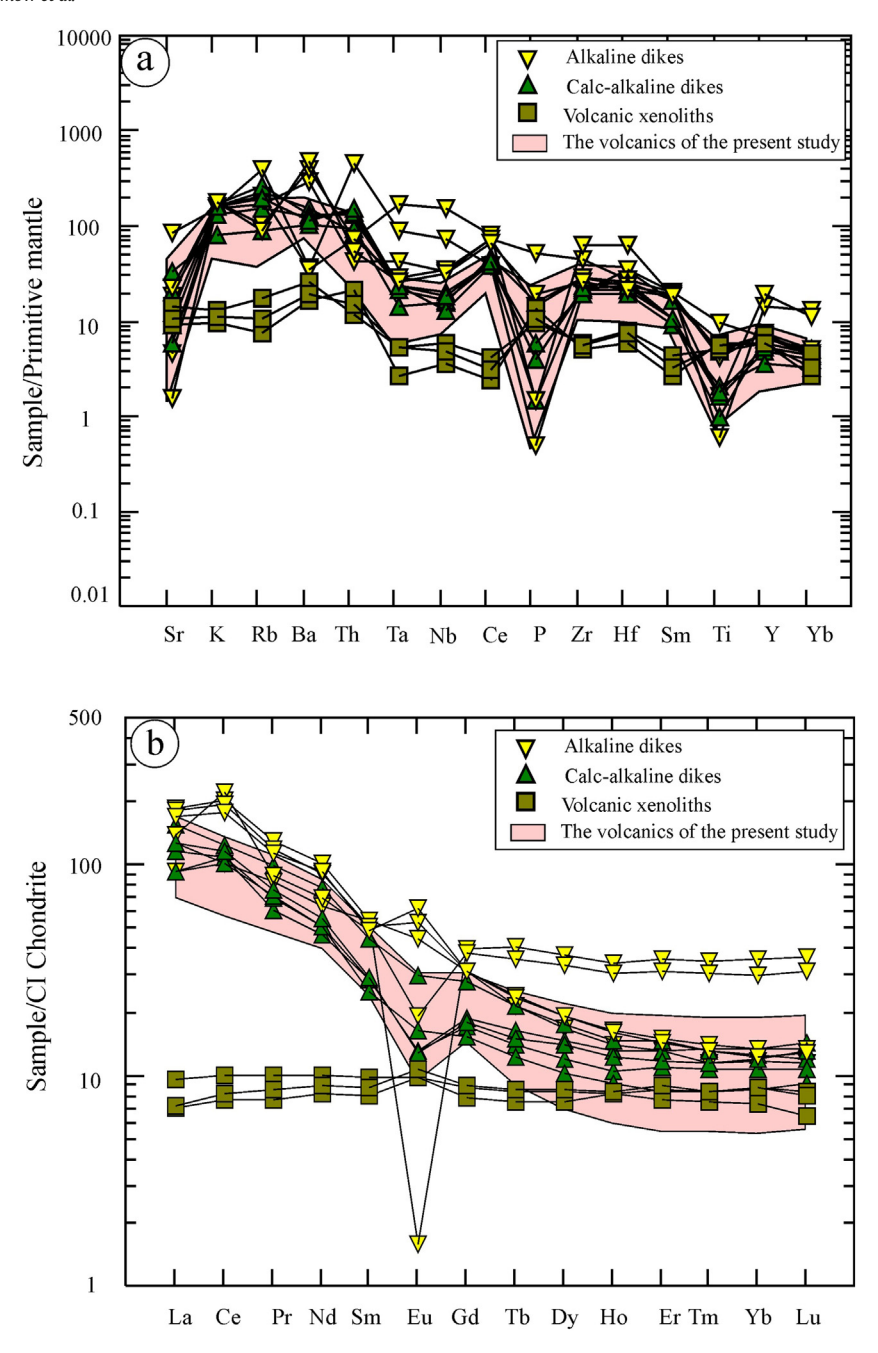


Fig. 11. Normalized trace-element diagrams for the dike and xenolith samples from the study area: (a) primitive-mantle normalized trace element patterns and (b) CI-Chondrite normalized REE plots. Symbols as in Fig. 6.

mature, it remained stubbornly low-K (Abdel-Karim et al. 2019), unlike the medium- to high-K character of the Guruf volcanics. Maurice et al. (2018) reasoned from inconsistencies between the observed evolution of Mg# and REE abundances and those expected for fractional crystallization to infer an evolving source within the suite. The Mg# results may have been affected by strong alteration of the basalts, by magma mixing, or by combining unrelated stratigraphic units. The slowly evolving REE contents during differentiation are common in all post-collisional plutonic and volcanic rocks in the ANS (Be'eri-Shlevin et al. 2011; Eyal et al. 2010); we model this feature below by appealing to apatite fractionation. Based on the present field work and geochemical data, we find that the Guruf volcanic suite lacks basaltic members and was emplaced in two cycles of eruption of medium- to high-K calc-alkaline volcanic rocks derived from a common source

The most primitive samples (basaltic andesite) in the Guruf volcanics have Mg# \leq 56, Ni \leq 90 µg/g, and Cr \leq 317 µg/g. Primary basaltic melts in equilibrium with residual mantle are expected to have high Ni and Cr contents (> 250 and > 1000 µg/g, respectively) and Mg# in the range 68–75 (Roeder and Emslie, 1970). Hence, there are no candidates for a primary mantle-derived melt among the Guruf rocks.

In the present work and many published reports (Be'eri-Shlevin et al. 2011; Obeid and Azer 2015), REE patterns and other features suggestive of subduction-related magmatism have been interpreted to reflect inheritance due to remelting of earlier arc-related material from the pre-collisional stage (850–740 Ma). Therefore, the proposed model for the genesis of the Guruf volcanics is partial melting of lower continental crust followed by ascent and fractionation at upper crustal levels. The most primitive members of the Guruf volcanics represented

Table 6REE concentrations of the dykes and volcanic xenoliths associated with Guruf volcanics, North Eastern Desert, Egypt.

Rock type	Dykes		Xenoliths										
	Alkaline d	ykes				Calc-alk	aline dykes						
Sample	GH9 ^a	GH14 ^a	Gh20 ^a	GH11 ^a	GH19 ^a	GH7 ^a	Gh17 ^a	Gh5 ^a	GH16 ^a	GH6 ^a	Xen.1	Xen.6	Xen.9
La	39.46	43.29	42.86	21.96	32.30	29.83	36.09	26.96	21.82	29.58	1.66	2.25	1.69
Ce	107.52	121.52	118.01	61.45	134.61	70.60	74.88	66.08	65.16	61.36	4.64	6.03	4.98
Pr	10.70	12.09	11.08	7.85	8.27	7.22	9.29	6.54	5.69	6.64	0.73	0.95	0.81
Nd	42.75	47.25	42.29	29.64	32.05	25.90	36.11	23.64	21.57	23.51	3.79	4.61	4.11
Sm	7.40	8.24	7.80	8.17	7.34	4.44	6.78	4.31	4.31	3.77	1.21	1.48	1.32
Eu	3.58	2.54	3.04	0.09	1.10	0.73	1.73	0.75	0.76	0.95	0.56	0.56	0.61
Gd	6.34	6.37	6.29	8.15	7.78	3.62	5.73	3.45	3.82	3.12	1.77	1.6	1.83
Tb	0.87	0.80	0.89	1.51	1.31	0.56	0.80	0.52	0.60	0.45	0.31	0.28	0.32
Dy	4.81	4.21	4.82	9.42	8.44	3.49	4.37	2.99	3.67	2.56	2.1	1.91	2.17
Но	0.89	0.79	0.92	1.90	1.70	0.69	0.83	0.59	0.74	0.51	0.46	0.46	0.47
Er	2.36	2.14	2.46	5.80	5.14	1.94	2.38	1.79	2.17	1.37	1.42	1.26	1.46
Tm	0.33	0.29	0.35	0.89	0.77	0.29	0.33	0.27	0.34	0.21	0.21	0.19	0.21
Yb	2.06	1.97	2.28	5.99	5.08	2.00	2.13	1.80	2.26	1.44	1.47	1.25	1.47
Lu	0.32	0.29	0.34	0.92	0.78	0.33	0.30	0.27	0.36	0.23	0.21	0.16	0.2
Eu/Eu*	1.60	1.07	1.33	0.03	0.44	0.55	0.85	0.60	0.58	0.84	1.17	1.11	1.20
(La/Yb) _n	12.93	14.86	12.69	2.48	4.30	10.07	11.48	10.12	6.52	13.90	0.76	1.22	0.78
(La/Sm) _n	3.36	3.32	3.47	1.70	2.78	4.24	3.36	3.95	3.20	4.95	0.87	0.96	0.81
(Gd/Lu) _n	2.39	2.71	2.26	1.09	1.23	1.36	2.31	1.56	1.29	1.67	1.03	1.23	1.12
(La/Lu) _n	12.46	15.41	12.89	2.45	4.27	9.38	12.18	10.19	6.16	13.19	0.81	1.44	0.87

^a Samples analyzed in Caltech (USA).

in our sample suite are basaltic andesites with ~54 wt% SiO₂ and ~ 5 wt% MgO; a plausible model for the origin of the suite must define conditions where such a liquid can coexist with residual amphibole. Such a condition was identified in the experimental study of Carroll and Wyllie (1989), who found that a Sierra Nevada (USA) tonalite (a continental arc rock) mixed with 10 wt% peridotite, in the presence of 10 wt% H_2O , has hornblende near the liquidus at 1.5 GPa and up to ~950 °C. Below this temperature, the MgO in the liquid rapidly decreases; above this temperature, hornblende melts out. At higher pressure, garnet occurs; at lower pressure, plagioclase becomes dominant. The TP10 composition studied by Carroll and Wyllie is a remarkably close match to the average Guruf basaltic andesite (Fig. 7). We suggest that it offers a guide to the conditions of formation of the primary magma for the Guruf volcanics: beneath the ~30 km ANS crust, a lower crustal delamination event led to sinking arc-affinity tonalite being mixed with asthenospheric peridotite and experiencing heating as it sank. Near 950 °C and 1.5 GPa, a liquid of basaltic andesite composition separated from an amphibole-bearing but plagioclase- and garnet-free residue and ascended back into the crust.

The extrusion of the Guruf volcanics was associated with extensive denudation of the pre-630 Ma orogenic edifice as well as the 630–600 Ma post-collisional products. The vertical displacements that drove such erosion may have been surface expressions of isostatic rebound due to thinning (and likely delamination) of the previously thickened lithosphere, facilitating the upwelling of hot asthenospheric material (e.g., Avigad and Gvirtzman 2009) and the rapid elevation of the lower crustal geotherm. This may have been the trigger for the transition into dominantly alkaline A-type magmatism at 600 Ma.

7.2. Geodynamic significance of adakitic lavas

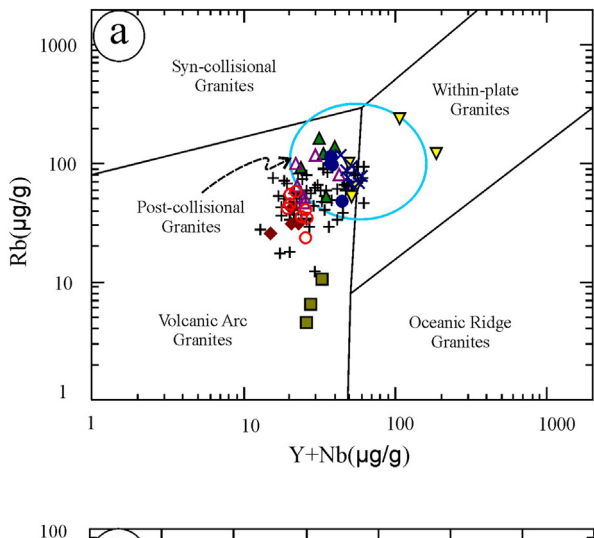
Adakites were originally interpreted as low-degree partial melts of subducted oceanic crust that interacted with mantle peridotite at high pressure, leaving a garnet-rich but plagioclase-poor residue that yields high Sr/Y and La/Yb ratios (Defant and Drummond 1990). However, the definition of adakite is geochemical rather than petrogenetic (Richards and Kerrich 2007) and volcanic rocks meeting the definition of adakite have been identified in a range of tectonic environments associated with a corresponding range of magmatic sources and processes. Therefore, the sources of individual suites of adakitic rocks have been debated extensively and a number of models for their

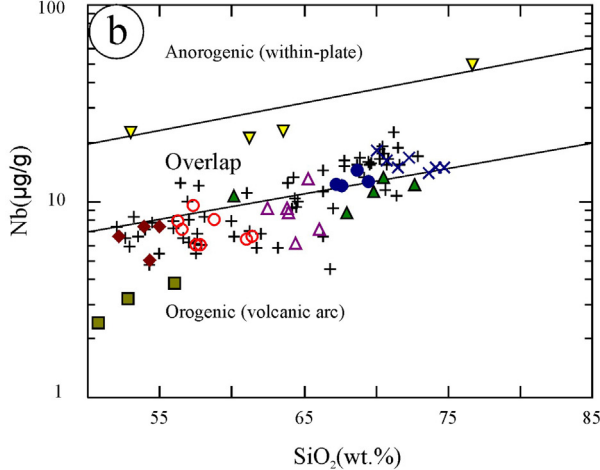
formation have been suggested (for review see Castillo 2012). Generally, such models divide into two main groups: (1) partial melting of an oceanic slab in an active subduction-related environment (e.g. Defant and Drummond 1990; Zhu et al. 2009) and (2) non-slab origins, wherein the adakite signature may be derived in garnet- or amphibole-bearing upper plate crust, by differentiation processes (such as fractional crystallization, magma mixing, or crustal contamination) or by anatexis of pre-existing crustal materials (Castillo 2012; Macpherson et al. 2006; Obeid and Azer 2015).

Many of the post-collisional calc-alkaline magmas in the ANS have adakitic affinity (Abdelfadil et al. 2018; Be'eri-Shlevin et al. 2011; Eliwa et al. 2006; Hargrove et al. 2006; Obeid and Azer 2015). Mirroring the global debate, many fundamentally different models for the origins of the ANS adakitic rocks have been suggested (Abdelfadil et al. 2018; Be'eri-Shlevin et al. 2011; Eliwa et al. 2006). Models differ in the expected time of the events that triggered melting: ≥ 630 Ma for the subducted ridge model (Avigad and Gvirtzman 2009) versus 610–600 Ma for delamination (Eyal et al. 2010; Moghazi 2003). They differ also in the source components; e.g., a broken oceanic slab (Moghazi 2003) versus mafic lower continental arc crust (Avigad and Gvirtzman 2009; Eyal et al. 2010).

Eliwa et al. (2006) suggested that a hot oceanic ridge was subducted (pre- or *syn*-collision) and then melted some 20 m.y. later, in a post-collisional regime, yielding the post-collisional adakitic volcanic rocks of southern Israel and the Eastern Desert. The lack of evidence for oceanic crust younger than ca. 690 Ma in the northern ANS (Stacey et al. 1984) does not support this model, even if the various adakitic post-collisional volcanic series are all assumed to be as old as ca. 630 Ma, which is probably not the case.

The Guruf adakitic volcanics have geochemical characteristics associated with upper plate crustal sources or interactions, which is consistent with a post-collisional setting: Mg# (<56), Cr (<10 μ g/g), and Ni (<90 μ g/g) contents are lower than those expected for primary adakite magma derived from partial melting of subducted oceanic crust that has only interacted with mantle wedge peridotite (e.g. Zhu et al. 2009). The need for crustal residence and evolution favors a model whereby the adakitic characteristics were acquired in the upper plate crust and makes it quite challenging to trace them back to primary slab or mantle derivation. Furthermore, the present volcanic suite, when plotted as either MgO (Condie 2005) or Mg# (Zhu et al. 2009) versus SiO₂, does not plot in the field of slab melting-related adakites (Fig. 13a, b).





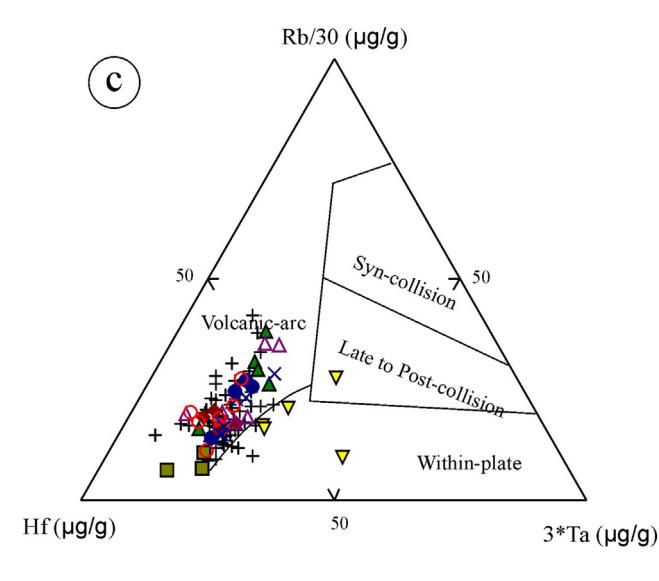


Fig. 12. Tectonomagmatic diagrams: (a) Yb + Nb vs. Rb (Pearce et al. 1984), with post-collisional granite field after Pearce (1996); (b) SiO₂ versus Nb (after Pearce and Gale 1977); and (d) Hf-Rb/30-3*Ta ternary (after Harris et al. 1986). Symbols as in Fig. 6.

According to Be'eri-Shlevin et al. (2011), post-collisional adaktitic volcanic rocks of the ANS simply require derivation from a source with garnet or amphibole in the residue. Thickened, mafic, lower continental crust may be partially melted (e.g., Moyen and Martin 2012) in the eclogite or garnet amphibolite stability fields, perhaps during

delamination (Gao et al. 2004). This mechanism is not feasible in situ where crust is less than ~30 km thick, typically the minimum depth of garnet amphibolite or eclogite-facies metamorphism (Macpherson et al. 2006). Garnet is increasingly abundant in mafic magmas at ≥40 km depth (Richards and Kerrich 2007) and increasingly likely to remain in the residue and retain HREE and Y after significant degrees of partial melting. The crust beneath the ANS is essentially mafic and has (today) an average thickness of 39 km in Saudi Arabia, rapidly thinning to 23-25 km along the Red sea coast and the margin of the Gulf of Agaba (Al-Damegh et al., 2005). That is, the ANS crust is at the present day only marginally thick enough for garnet to be a significant residual phase at the base of the crust and there is limited evidence for major crustal thinning associated with post-Neoproterozoic activity. Moreover, the moderately fractionated REE patterns of the Guruf volcanics (Fig. 10b), with undepleted and nearly flat HREE slopes, are inconsistent with batch melting of an eclogite source (e.g., Stern and Gottfried 1986). Therefore, the most primitive observed basaltic andesite is unlikely to have been derived directly from partial melting of garnet amphibolite or eclogite facies rocks in-place in stable thickened lower crust.

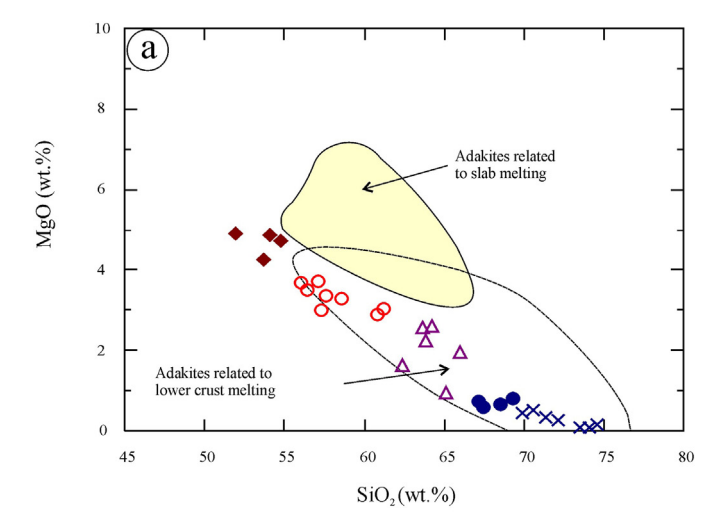
A simpler model that would explain the post-collisional adakitic rocks of the ANS in general, and the Guruf volcanism in particular, is melting of delaminated lower crust (Kay and Kay 1993). Heating of delaminated lower crust in the mantle would explain the high degrees of melting needed to produce basaltic andesites (requiring up to 25% melting of eclogite; e.g., Stern and Gottfried 1986). Independent geodynamic arguments in favor of delamination of lower crust in the ANS at this time (630–590 Ma) have been recently discussed by many authors (Abdelfadil et al. 2018; Avigad and Gvirtzman 2009; Farahat and Azer 2011; Moghazi 2003; Obeid and Azer 2015). The melting of delaminated lower crust is more consistent with the tectonic setting of the post-collisional adakitic volcanic sequences than the oceanic ridge model of Eliwa et al. (2006). The geochemical signatures of adakitic magma require sufficiently high pressures and water contents to suppress residual plagioclase (Macpherson et al. 2006).

Delamination and the ensuing isostatic rebound would trigger an extensional tectonic regime that would open conduits for smalldegree alkaline magmas and, at the surface, cause development of basins to provide accommodation space for volcano-sedimentary accumulation. Indeed, there is a record of peak extensional tectonics in the northernmost ANS at ca. 600 Ma (Stern et al., 1984). The proposed geodynamic model for generation of the studied volcanic sequences involved the following steps, beginning some tens of m.y. after the end of subduction in the northern ANS: (1) delamination of lithospheric mantle and tonalitic lower arc crust, triggering (2) partial melting of the delaminated lower crust as it undergoes amphibolite-grade metamorphism and heating by intimate mixing with ascending asthenosphere, followed by (3) the onset of extension and subsidence, (4) ascent of basaltic andesite together with fractional crystallization to form the andesite and dacite of the lower Guruf volcanics, and (5) after a hiatus and further fractionation, renewed eruption of the upper felsic volcanic cycle of rhyodacite and rhyolite.

7.3. Physicochemical conditions of evolution and alteration

Mafic igneous minerals are sensitive to variations in both the chemistry and the P-T-a-t0 $_2$ conditions of crystallization and so can be used in some cases to estimate the P-t0 conditions early in magmatic evolution (e.g., Lindsley 1983; Ridolfi et al. 2010). The Wo-En-Gs clinopyroxene quadrilateral was contoured for temperature estimation by Lindsley (1983). The present data, drawn from augite in the basaltic andesite and andesite samples, plot mainly between the 800 and 1000 °C contours (Fig. 5a).

The compositions of primary hornblende have been used by many authors for geothermometry, oxybarometry, and geobarometry of igneous rocks (e.g., Ridolfi et al. 2010). Application of the temperature-sensitive Si-index for amphibole from Ridolfi et al.



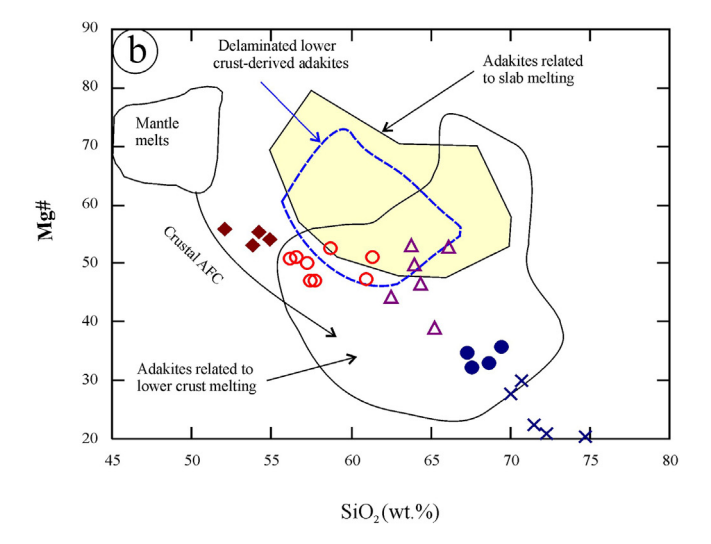


Fig. 13. Discrimination diagrams for different adakite source models: (a) MgO vs. SiO₂, (b) Mg# vs. SiO₂. Crustal AFC curve according to Stern and Kilian (1996). Fields indicating mantle melt, adakites related to slab melting, lower-crustal melting, and delaminated lower crust-derived adakites are according to Gao et al. (2004), Condie (2005), and Zhu et al. (2009). Symbols as in Fig. 6.

(2010) gives crystallization temperature of primary hornblende 807–944 °C in basaltic andesite, 814–855 °C in andesite, and 781–835 °C in dacite, with typical uncertainty of ± 22 °C. The estimated pressures are 120–345 MPa in basaltic andesite, 108–346 MPa in andesite, and 91–145 MPa in dacite. Despite significant uncertainty, the amphibole compositions appear to record progressive cooling and ascent of the magma as it evolves. The oxygen-sensitive Fe/(Fe + Mg) versus Al^IV amphibole discrimination diagram (Anderson and Smith 1995) shows that the primary amphiboles in the Guruf volcanics crystallized under high $f\mathrm{O}_2$ conditions (Fig. 14).

The observed compositions of chlorite depend, most probably, on the nature of their precursor ferromagnesian minerals and the conditions of alteration (temperature, composition, and redox state of aqueous solutions), as discussed by several investigators (e.g., Abdel-Rahman 1995; Cathelineau 1988; Kranidiotis and MacLean 1987). Kranidiotis and MacLean (1987) calibrated an empirical chlorite geothermometer for estimating the temperature of chlorite formation by replacement of mafic minerals. Calculated results from this formulation are less than 306 °C (supplementary table 6SD), consistent with the stability limits of chlorite and the petrographic evidence that chlorite formation happened at a late stage. This supports the distinction we

make in this work between the minor low-temperature alteration that has affected the Guruf volcanics and the greenschist-facies or higher metamorphism that is characteristic of the subduction-related rocks of the ANS.

7.4. Fractional crystallization

The systematic variation of major and trace element contents of the Guruf volcanics (Figs. 7, 8) can be interpreted in terms of magmatic differentiation processes. Decreasing $Fe_2O_3^*$, MgO, CaO, TiO_2 , P_2O_5 and Sr coupled with increasing Zr, Rb, Y, Nb contents are all consistent with fractionation of plagioclase, apatite and Fe—Ti oxides. Likewise, the increasing development of strong negative P, Ti, and Sr anomalies in the normalized trace element patterns of dacite, rhyodacite and rhyolite samples (Fig. 10a) indicates fractionation of these phases. The progression from positive Eu anomalies in basaltic andesite (suggesting the absence of residual plagioclase in the source), to small negative Eu anomalies in dacite and onward to large negative Eu anomalies in the rhyolite also indicates steady removal of Ca-bearing phases such as plagioclase and apatite.

Middle and heavy-REE patterns are good indicators of the roles of amphibole and garnet, respectively, in a magmatic system (Castillo 2012; Defant and Drummond 1990). The concave-up REE patterns of basaltic andesite (Fig. 10b) imply a role for amphibole, likely as a residual phase in the source (Be'eri-Shlevin et al. 2011). The increases in HREE with evolution and the persistence of low MREE/HREE requires the absence of garnet fractionation and allows the possibility of ongoing amphibole fractionation from a hydrous parental magma.

Inspired by the presence of magmatic amphibole, by the evidence of pressures decreasing from ~300 MPa to ~125 MPa during evolution, and by the high fO2 recorded by the amphibole, we constructed a quantitative model of evolution using the rhyoliteMELTS 1.0.2 model (Ghiorso and Gualda, 2013) and the easyMelts 0.2.4 and alphaMELTS 1.9 interfaces. The model is assumed to begin from the average composition of the basaltic andesite samples on its liquidus (1155 °C) at 300 MPa, with 2 wt% dissolved H_2O on the nickel-nickel oxide (NNO) oxygen buffer. Fractionation proceeds in 1 °C cooling steps with 0.4 MPa of decompression at each step, terminating at 725 °C and 125 MPa. The liquid line of descent generated by this simple model captures many significant features of the major and trace element evolution of the suite (Figs. 7, 8). In particular, the steepness of enrichment of incompatible elements is matched or exceeded by the model with no need for assimilation of an enriched component. However, there are four features that

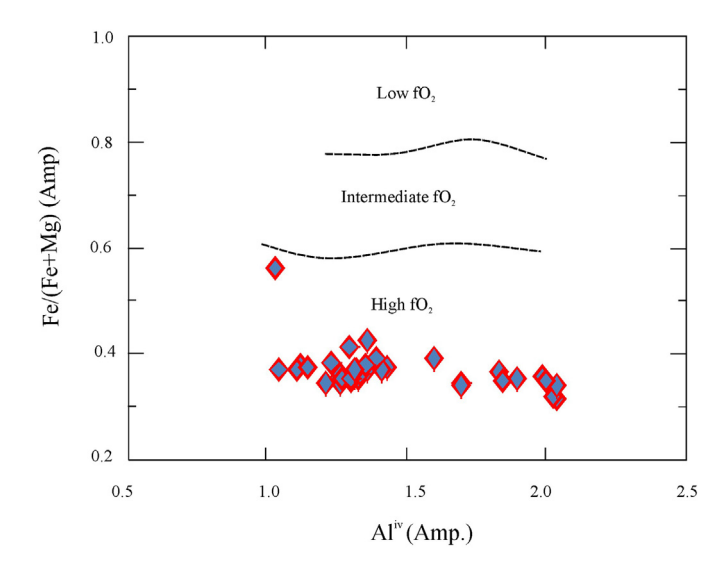


Fig. 14. Fe/(Fe + Mg) vs. Al^{IV} diagram for primary amphibole (Anderson and Smith 1995).

are not captured by the model: CaO does not decrease steeply enough with increasing SiO₂, P₂O₅ has altogether the wrong trend, the LREE act more incompatibly than the HREE in the model (whereas the data show the opposite, Fig. 10), and the Eu anomalies predicted in the rhyolite are too small. All of these features can be simultaneously remedied simply by adding a larger quantity of fractionating apatite than is predicted by the model. It has been frequently noted since the rhyoliteMELTS calibration came out that it underpredicts the stability of apatite in felsic systems. Hence, we artificially added more apatite to the fractionating assemblage; a constant rate of apatite fractionation (0.0004 wt%/°C) simultaneously fits the CaO, P₂O₅, LREE, and Eu anomaly trends (Figs. 7, 8, 10c).

With the apatite adjustment, the simple decompression and fractional crystallization model is successful at explaining most features of the major and trace element chemistry, so we conclude that the whole-rock data do not require assimilation, recharge, or other complexity during magmatic evolution of the Guruf volcanic suite. However, oscillatory zoning in plagioclase in the andesite and dacite (Fig. 4c, d) does suggest the occurrence of fluctuations in magmatic conditions (pressure, temperature and H₂O content), which may indicate that recharge or mixing events did occur. On several variation diagrams, including those for Al₂O₃, Fe₂O₃*, MgO, and Na₂O, the data trend is straighter than the somewhat curved model liquid line of descent; the intermediate compositions could therefore be explained by a process of recharge of the fractionated magma by more primitive material entering the magma chamber. Studies of Dokhan volcanics at other localities in the Eastern Desert and Sinai have frequently called for a role for crustal contamination accompanying fractional crystallization (e.g., Abdel Rahman, 1996; Mohamed et al., 2000; Moghazi 2003; Eliwa et al. 2006; Obeid and Azer 2015). There is no evidence locally of over-enrichment in incompatible elements, so we consider the present suite to be permissive of a magmatic evolution without contamination, but we also do not rule out some amount of contamination.

7.5. Collision of East and West Gondwana

The ANS developed over a protracted period of ~300 Ma, passing through a series of distinct stages (Stern, 1994; Stern and Johnson 2010; Fritz et al. 2013): rifting and break-up of Rodinia into East and West Gondwana fragments sometime in Tonian time, a prolonged episode of formation of island arc terranes and their accretion from ~800–670 Ma, and reassembly of East and West Gondwana and intervening fragments by a continent-continent collision at ~630 Ma. Several intraoceanic subduction zones now incorporated in the ANS were active from 870 to 630 Ma. In Sinai, Eyal et al. (2014) concluded that the last (Kid) island arc in the northern ANS existed from ~640 to ~620 Ma, implying that the Mozambique Ocean persisted (at least locally) until ~620 Ma.

The collision between East and West Gondwana was a complex and lengthy process and it is challenging to interpret the age of any particular sample as the time of collision or even to argue that there was a single collision time (Andresen et al. 2009; Fritz et al. 2013; Stern and Johnson 2010). At the largest scale, there was a collision of two main fragments, East and West Gondwana, but along the whole length of the suture this event was diachronous and, given the irregular shapes of the continental margins, the age of "final collision" in one area may not preclude the continuing existence of open ocean elsewhere along the front (Fritz et al. 2013). There was a lengthy series of small and large terrane collisions throughout the whole period from ~850–620 Ma (Fritz et al. 2013).

However, many published studies have attempted to define the general chronology of the collision on the basis of local or regional studies. This kind of reasoning has led several authors to assign the high-K calcalkaline Dokhan volcanics series in the Eastern Desert of Egypt to the pre-collisional phase of ANS development (Maurice et al. 2018). This interpretation is generally based on geochronological correlation between

the Dokhan volcanic rocks and various deformed granite plutons, rather than on structural, stratigraphic, or metamorphic evidence indicating that the Dokhan lavas themselves were caught up in collisional deformation after their eruption, Andresen et al. (2009), for example, studied a certain area (Meatig) in the Eastern Desert of Egypt and found that deformation of I-type granite occurred at 605-600 Ma. From this evidence, they reasoned that collision between East and West Gondwana occurred at this late time, younger than the Dokhan volcanics and supporting their assignment to a pre-collisional phase. Without questioning the accuracy of the age of deformation of this granite, we must still ask whether it supports a broad regional interpretation. Deformation of various rock types may occur after collision and postcollisional plutons may inherit geochemical characteristics from earlier island arc stages. Hence, the measured age may not date the terminal collision locally, the deformed pluton may not be an island-arc stage pluton, and a local collision may not constrain the end of collisional activity elsewhere. We find the absence of deformation or metamorphism of the Dokhan sequence itself to be the most compelling evidence that Dokhan volcanics are post-collisional.

7.6. Existence of old continental crust beneath the ANS

The ANS is a product of the Neoproterozoic East African orogeny (870-550 Ma; Stern, 1994) and several authors have argued that the ANS was entirely juvenile material, with no incorporation of pre-Neoproterozoic crust (Stern, 1994; Maurice et al. 2018). However, a large number of pre-870 Ma inherited zircons (0.9-3.0 Ga) have been found in ANS magmas (e.g., Hargrove et al. 2006; Breitkreuz et al. 2010; Stern et al., 2010; Be'eri-Shlevin et al. 2011) and sediments (Li et al. 2018; Samuel et al. 2011; Wilde and Youssef 2002). Thus, other authors (e.g. El-Gaby et al. 1988; Khudeir et al., 2008; Li et al. 2018) have judged that extensive tracts of pre-Neoproterozoic continental crust exist beneath the Pan-African rocks of the ANS, at least in the Eastern Desert. Some authors (e.g., Liégeois and Stern 2010) have attempted to reconcile these views by stressing the durability and inheritability of zircons, such that pre-Neoproterozoic zircons need not require the presence of extensive tracts of older crust. However, the oxygen isotope compositions of zircons are relatively easy to modify (Cherniak and Watson 2003); old zircons that retain crustal oxygen isotope signatures likely were never recycled into the mantle and transported magmatically into juvenile crust. Thus Stern et al. (2010) stated that "it seems clear that ~1 Ga crust can be found near the Sa'al-Zaghra region of the Sinai Peninsula".

The high-grade gneisses and migmatites in the Eastern Desert occupy the lowest stratigraphic position, making them the substratum of all other units (El-Gaby et al. 1988; Li et al. 2018). Some authors have argued that these high-grade gneisses and migmatites represent an easterly extension of the Sahara Metacraton, remobilized and exposed in tectonic windows during the East African orogeny (e.g., Khudeir et al., 2008). On the other hand, late Neoproterozoic ages for high-grade gneisses in the northwestern ANS (e.g., Andresen et al. 2009; Liégeois and Stern 2010) have supported the contrary idea that they are part of the juvenile ANS crust, in spite of the older zircons (Be'eri-Shlevin et al., 2011). Azer and Asimow (2021) preferred the classical interpretation of these gneisses and sheared granites as cratonic, arguing that the Pan-African ages, especially in the northwestern part of the ANS, date episodes of metamorphism rather than protolith ages.

Maurice et al. (2018) claimed that the Dokhan volcanic rocks of the Eastern Desert developed in a subduction zone environment and preferred an intraoceanic arc setting over an active continental margin setting due to the absence of isotopic evidence for involvement of old continental crust. However, there is in fact significant evidence for the involvement of old continental crust in the generation of Dokhan volcanics (Breitkreuz et al. 2010; Stern et al. 2010; Be'eri-Shlevin et al., 2011). Li et al. (2018) studied, for example, a ~ 755 Ma rhyolite cobble from the Atud Formation in the Eastern Desert, whose exclusively negative

zircon $\epsilon_{\rm Hf}(t)$ values indicate a heterogeneous source enriched in Hf and not a juvenile oceanic arc source. Melting of a Paleoproterozoic-Archean protolith at ca. 755 Ma (Li et al. 2018) shows that the subduction stage of the ANS mobilized material of older continental crust origin and confirms the presence of such crust beneath the ANS.

8. Summary

The Guruf volcanics represent post-collisional magmatic activity following the assembly of the northernmost segment of the ANS. The two genetically related pulses together span a wide range of compositions (52.0–74.7 wt% $\rm SiO_2$) without any compositional gaps. They evolved from adakitic medium-K calc-alkaline rocks towards alkaline high-K character with progressive ascent and fractional crystallization. The metavolcanic xenoliths within the granodiorite are tholeitic, with very low $\rm K_2O$ and unfractionated REE and trace element patterns; they are not related to the Guruf volcanics and instead appear similar to the island-arc stage Shadli metavolcanics. Hence, they do not show that the granodiorite postdates the Guruf volcanics. The field relations indicate the opposite.

Primitive mantle-normalized multi-element diagrams show that the Guruf volcanics are enriched in large ion lithophile elements (LILE) relative to high field strength elements (HFSE), with significant troughs in Sr, P and Ti in the rhyodacite and rhyolite. All the Guruf volcanic rocks are LREE-enriched relative to HREE, but the patterns become less fractionated with progressive evolution, contrary to the standard expectations of simple fractional crystallization. The patterns are well-explained by the quantity of apatite fractionation required to match the Ca and P trends in the data. The consistently low MREE/HREE and flat HREE patterns indicate residual amphibole in the source of the basaltic andesites and rule out garnet fractionation.

On most tectonic setting discrimination diagrams, the Guruf volcanics lie between volcanic arc and within-plate fields. Throughout the ANS, this feature is characteristic of the post-collisional tectonic setting; true island-arc stage subduction-related magmas plot clearly within the volcanic arc fields. The evidence of subduction influence in the geochemistry of these lavas, despite their post-collisional setting, is interpreted to reflect remelting of previously formed arc material ca. 750–650 Ma in age.

The most likely source and setting for generation of the primitive basaltic andesite magma was lower crust undergoing high-P metamorphism and heating during delamination. Experimental studies show a narrow window near 950 °C, 1.5 GPa, 10% mixing with peridotite, and 10 wt% $\rm H_2O$, where tonalite could melt to produce basaltic andesite with residual amphibole. Such conditions could occur if lower arccrust material were heated as it delaminated and sank into the asthenosphere to a depth of ~50 km. Cooling during ascent and simple fractional crystallization provide a working model for evolution through the andesite and dacite of the lower Guruf volcanics. After a hiatus and continued fractionation, renewed eruption of the upper volcanic cycle emplaced the rhyodacite and rhyolite.

Declaration of Competing Interest

The authors declare that they have no known competing financial interests or personal relationships that could have appeared to influence the work reported in this paper.

Acknowledgements

The authors would like to extend their appreciation and gratitude to the King Saud University for funding and supporting this work through Researchers Supporting Project number (RSP-2020/151), King Saud University, Riyadh, Saudi Arabia. PDA's participation is supported by NSF award 1947616. We thank Einari Suikkanen for creating and sharing the easyMelts interface and Paula Antoshechkina for supporting the alphaMELTS trace element modeling capability. Finally, thorough reviews by the two reviewers as well as comments by Prof. Michael Roden (editor) greatly improved the present version of the manuscript.

Appendix A. Supplementary data

Supplementary data to this article can be found online at https://doi.org/10.1016/j.lithos.2021.106051.

References

- Abdel Rahman, A.M., 1996. Pan-African volcanism: petrology and geochemistry of the Dokhan Volcanic suite in the northern Nubian Shield. Geol. Mag. 133, 17–31.
- Abdelfadil, K.M., Obeid, M.A., Azer, M.K., Asimow, P.D., 2018. Late Neoproterozoic adaktitic lavas in the Arabian-Nubian shield, Sinai Peninsula, Egypt. J. Asian Earth Sci. 158, 301–323
- Abdel-Karim, A.M., Ali, S., El-Awady, A., Elwan, W., Khedr, M.Z., Tamura, A., 2019. Mineral and bulk-rock chemistry of Shadli bimodal metavolcanics from Eastern Desert of Egypt: Implication for tectonomagmatic setting and Neoproterozoic continental growth in the Arabian-Nubian Shield. Lithos 338, 204–217.
- Abdel-Rahman, A.M., 1995. Chlorites in a spectrum of igneous rocks: mineral chemistry and paragenesis. Mineral. Mag. 59, 129–141.
- Abu El-Enen, M.M., Lorenz, J., Ali, K.A., von Seckendorff, V., Okrusch, M., Schüssler, U., Brätz, H., Schmitt, R.T., 2018. A new look on Imperial Porphyry: a famous ancient dimension stone from the Eastern Desert of Egypt—petrogenesis and cultural relevance. Int. J. Earth Sci. 7, 2393–2408.
- Al-Damegh, K., Sandvol, E., Barazangi, M., 2005. Crustal structure of the Arabian plate: new constraints from the analysis of teleseismic receiver functions. Earth Planet. Sci. Lett. 231 (3–4), 177–196.
- Ali, B.H., 2015. SHRIMP U-Pb zircon geochronology: evidence for emplacement time of some granitoids north Eastern Desert, Egypt. Arab. J. Geosci. 8, 5465–5474.
- Ali, K.A., Azer, M.K., Gahlan, H.A., Wilde, S.A., Samuel, M.D., Stern, R.J., 2010. Age constraints on the formation and emplacement of Neoproterozoic ophiolites along the Allaqi-Heiani Suture, South Eastern Desert of Egypt. Gondwana Res. 8 (4), 583–595.
- Ali, K.A., Andresen, A., Stern, R.J., Manton, W.I., Omar, S.A., Maurice, A.E., 2012. U-Pb zircon and Sr-Nd-Hf isotopic evidence for a juvenile origin of the ~634 Ma El-Shalul Granite, Central Eastern Desert, Egypt. Geol. Mag. 149, 783–797.
- Anderson, J.L., Smith, D.R., 1995. The effects of temperature and fO2 on the Al-in-hornblende barometer. Am. Mineral. 80, 549–559.
- Andresen, A., Abu El-Rus, M.A.A., Myhre, P.I., Boghdady, G.Y., Corfu, F., 2009. U–Pb TIMS age constraints on the evolution of the Neoproterozoic Meatiq Gneiss dome, Eastern Desert, Egypt. Int. J. Earth Sci. 98 (3), 481–497.
- Avigad, D., Gvirtzman, Z., 2009. Late Neoproterozoic rise and fall of the northern Arabian– Nubian shield: the role of lithospheric mantle delamination and subsequent thermal subsidence. Tectonophysics 477, 217–228.
- Azer, M.K., Asimow, P.D., 2021. Petrogenetic Evolution of the Neoproterozoic Igneous Rocks of Egypt. The Geology of the Egyptian Nubian Shield. Springer, Cham, pp. 343–382.
- Azer, M.K., Farahat, E.S., 2011. Late Neoproterozoic volcano-sedimentary succession of Wadi Rufaiyil, southern Sinai, Egypt: a case of transition from late- to post-collisional magmatism. J. Asian Earth Sci. 42, 1187–1203.
- Azer, M.K., Abu El-Ela, F.A., Ren, M., 2012. The petrogenesis of late Neoproterozoic mafic dike-like intrusion in South Sinai, Egypt. J. Asian Earth Sci. 54, 91–109.
- Basta, F.F., Maurice, A.E., Bakhit, B.R., Azer, M.K., El-Sobky, A.F., 2017. Intrusive rocks of the Wadi Hamad Area, North Eastern Desert, Egypt: Change of magma composition with maturity of Neoproterozoic continental island arc and the role of collisional plutonism in the differentiation of arc crust. Lithos 288-289, 248-263.
- Be'eri-Shlevin, Y., Samuel, M.D., Azer, M.K., Rämö, O.T., Whitehouse, M.J., Moussa, H.E., 2011. The late Neoproterozoic Ferani and Rutig volcano-sedimentary successions of the northernmost Arabian-Nubian Shield (ANS): New insights from zircon U-Pb geochronology, geochemistry and O-Nd isotope ratios. Precambrian Res. 188, 21–44.
- Breitkreuz, C., Eliwa, H., Khalaf, I., El Gameel, K., Bühler, B., Sergeev, S., Larionov, A., Murata, M., 2010. Neoproterozoic SHRIMP U-Pb zircon ages of silica-rich Dokhan Volcanics in the North Eastern Desert, Egypt. Precambrian Res. 182, 163–174.
- Carroll, M.J., Wyllie, P.J., 1989. Experimental phase relations in the system tonalite-peridotite-H₂O at 15 kb; Implications for assimilation and differentiation processes near the crust-mantle boundary. J. Petrol. 30 (6), 1351–1382.
- Castillo, P.R., 2012. Adakite petrogenesis. Lithos 134–135, 304–316.
- Cathelineau, M., 1988. Cation site occupancy in chlorites and illites as a function of temperature. Clay Miner. 23, 471–485.
- Cherniak, D.J., Watson, E.B., 2003. Diffusion in zircon. Rev. Mineral. Geochem. 53 (1), 113–143.
- Condie, K.C., 2005. TTGs and adakites: are they both slab melts? Lithos 80, 33-44.
- Cox, K.G., Bell, J.D., Pankhurst, R.J., 1979. The Interpretation of Igneous Rocks. Allen & Unwin, London, p. 450.
- Defant, M.J., Drummond, M.S., 1990. Derivation of some modern arc magmas by melting of young subducted lithosphere. Nature 347, 662–665.
- El-Gaby, S., List, F.K., Tehrani, R., 1988. Geology, evolution and metallogenesis of the Pan-African belt in Egypt. The Pan-African belt of Northeast Africa and Adjacent Areas: Tectonic Evolution and Economic Aspects of a Late Proterozoic Oregon, pp. 17–68.

- El-Gaby, S., Khudier, A.A., Abdel Tawab, M., Atalla, R.F., 1991. The metamorphosed volcano-sedimentary succession of Wadi Kid, southeastern Sinai, Egypt. Annals of Geological Survey of Egypt XVII, pp. 19–35.
- Eliwa, H.A., Kimura, J.I., Itaya, T., 2006. Late Neoproterozoic Dokhan Volcanics, North Eastern Desert, Egypt: geochemistry and petrogenesis. Precambrian Res. 151, 31–52.
- Eliwa, H.A., El-Bialy, M.Z., Murata, M., 2014. Ediacaran post-collisional volcanism in the Arabian-Nubian Shield: the high-K calc-alkaline Dokhan Volcanics of Gabal Samr El-Qaa (592 ± 5 Ma), North Eastern Desert, Egypt. Precambrian Res. 246, 180-207.
- Eyal, M., Litvinovsky, B., Jahn, B.M., Zanvilevich, A., Katzir, Y., 2010. Origin and evolution of post-collisional magmatism: coeval Neoproterozoic calc-alkaline and alkaline suites of the Sinai Peninsula. Chem. Geol. 269, 153–179.
- Eyal, M., Be'eri-Shlevin, Y., Eyal, Y., Whitehouse, M.J., Litvinovsky, B., 2014. Three successive Proterozoic island arcs in the northern Arabian-Nubian Shield: evidence from SIMS U-Pb dating of zircon. Gondwana Res. 25, 338–357.
- Farahat, E.S., Azer, M.K., 2011. Post-collisional magmatism in the northern Arabian-Nubian Shield: the geotectonic evolution of the alkaline suite at Gebel Tarbush area, South Sinai, Egypt. Geochemistry 71 (3), 247–266.
- Fritz, H., Abdelsalam, M., Ali, K.A., Bingen, B., Collins, A.S., Fowler, A.R., Ghebreab, W., Hauzenberger, C.A., Johnson, P.R., Kusky, T.M., Macey, P., Muhongo, S., Stern, R.J., Viola, G., 2013. Orogen styles in the East African Orogen: a review of the Neoproterozoic to Cambrian tectonic evolution. J. Afr. Earth Sci. 86, 65–106.
- Gahlan, H., Azer, M.K., Asimow, P., Al-Kahtany, K., 2016. Late Ediacaran post-collisional Atype syenites with shoshonitic affinities, northern Arabian-Nubian Shield: a possible mantle-derived A-type magma. Arab. J. Geosci. 9 (12), 603.
- Gao, S., Rudnick, R.L., Yuan, H.L., Liu, X.M., Xu, W.L., Lin, W.L., Ayers, J., Wang, X.C., Wang, Q.H., 2004. Recycling lower continental crust in the North China Craton. Nature 432, 892–897.
- Ghiorso, M.S., Gualda, G.A., 2013. A method for estimating the activity of titania in magmatic liquids from the compositions of coexisting rhombohedral and cubic irontitanium oxides. Contribut. Mineral. Petrol. 165 (1), 73–81.
- Hargrove, U., Stern, R., Kimura, J.-I., Manton, W., Johnson, P., 2006. How juvenile is the Arabian–Nubian Shield? Evidence from Nd isotopes and pre-Neoproterozoic inherited zircon in the Bi'r Umq suture zone, Saudi Arabia. Earth Planet. Sci. Lett. 252 (3), 308–326.
- Harris, N.B., Pearce, J.A., Tindle, A.G., 1986. Geochemical characteristics of collision-zone magmatism. In: Coward, M.P., Ries, A.C. (Eds.), Collision Tectonics. Geological Society of London, Special Publications 19, pp. 67–81.
- Hey, M.H., 1954. A new review of the chlorites. Mineralo. Magazine 30, 277-292.
- Hossny, H.A.H., 2008. Geochemistry, Petrogenesis and Geochemical Exploration of the Rock Association at Wadi Hamad District, North Eastern Desert, Egypt. Ph. D. Thesis. Alexandria University, Egypt, p. 246.
- Irvine, T.N., Baragar, W.R.A., 1971. A guide to the chemical classification of the common volcanic rocks. Can. J. Earth Sci. 8, 523–548.
- Johnson, P.R., Kattan, F., 2007. Geochronologic Dataset for Precambrian Rocks in the Arabian Peninsula. A Catalogue of U–Pb, Rb–Sr, Ar–Ar, and Sm–Nd Ages: Saudi Geological Survey Open-File report SGS-OF-2007-3. p. 21.
- Johnson, P.R., Woldehaimanot, B., 2003. Development of the Arabian-Nubian Shield: Perspectives on accretion and deformation in the East African Orogen and the assembly of Gondwana. In: Yoshida, M., Windley, B.F., Dasgupta, S. (Eds.), Proterozoic East Gondwana: Supercontinent Assembly and Breakup. Geological Society of London, Special Publication, pp. 289–325.
- Kay, R.W., Kay, S.M., 1993. Delamination and delamination magmatism. Tectonophysics 219, 177–189.
- Keeditse, M., Rajesh, H.M., Belyanin, G.A., Fukuyama, M., Tsunogae, T., 2016. Primary magmatic amphibole in Archaean meta-pyroxenite from the central zone of the Limpopo complex, South Africa. South Afr. J. Geol. 119 (4), 607–622.
- Khudeir, A.A., Abu El-Rus, M.A., El-Gaby, S., El-Nady, O., Bishara, W.W., 2008. Sr-Nd isotopes and geochemistry of the infrastructural rocks in the Meatiq and Hafafit core complexes, Eastern Desert, Egypt: Evidence for involvement of pre-eoproterozoic crust in the growth of Arabian-Nubian Shield. Island Arc 17 (1), 90–108.
- Kranidiotis, P., MacLean, W.H., 1987. Systematics of chlorite alteration at the Phelps Dodge massive sulfide deposit, Matagami, Quebec. Econ. Geol. 82, 1898–1911.
- Le Bas, M.J., 1962. The role of aluminum in igneous clinopyroxenes with relation to their parentage. Am. J. Sci. 260, 267–288.
- Leterrier, J., Maury, R.C., Thonon, P., Girard, D., Marchal, M., 1982. Clinopyroxene composition as a method of identification of the magmatic affinities of paleo-volcanic series. Earth Planet. Sci. Lett. 59 (1), 139–154.
- Li, X.H., Abd El-Rahman, Y., Abu Anbar, M., Li, J., Ling, X.X., Wu, L.G., Masoud, A.E., 2018. Old continental crust underlying juvenile oceanic arc: evidence from northern Arabian-Nubian Shield, Egypt. Geophys. Res. Lett. 45 (7), 3001–3008.
- Liégeois, J.P., Stern, R.J., 2010. Sr–Nd isotopes and geochemistry of granite-gneiss complexes from the Meatiq and Hafafit domes, Eastern Desert, Egypt: no evidence for pre-Neoproterozoic crust. J. Afr. Earth Sci. 57 (1–2), 31–40.
- Liégeois, J.P., Navez, J., Black, R., Hertogen, J., 1998. Contrasting origin of post-collision high-K calc-alkaline and shoshonitic versus alkaline and peralkaline granitoids. The use of sliding normalization. Lithos 45, 1–28.
- Lindsley, D.H., 1983. Pyroxene thermometry. Am. Mineral. 68, 477–493.
- Macpherson, C.G., Dreher, S.T., Thirlwall, M.F., 2006. Adakites without slab melting: High pressure differentiation of island arc magma, Mindanao, the Philippines. Earth Planet. Sci. Lett. 243, 581–593.
- Maurice, A.E., Bakhit, B.R., Basta, F.F., Asimow, P.D., Wälle, M., Azer, M.K., El-Sobky, A.F., 2018. The last subduction-related volcanism in the northern tip of the Arabian- Nubian Shield: a Neoproterozoic arc preceding the terminal collision of East and West Gondwana. Precambrian Res. 310, 256–277.

- Moghazi, A.M., 2003. Geochemistry and petrogenesis of a high-K calc-alkaline Dokhan Volcanic suite, south Safaga area, Egypt: the role of late Neoproterozoic crustal extension. Precambrian Res. 125, 161–178.
- Moghazi, A.M., El-Sayed, M.M., Arslan, A.I., Hosny, H., 2004. Geochemistry and petrogenesis of the late Neoproterozoic granitoids at Wadi Hamad, Northern Eastern Desert, Egypt. 6th International Conference on Geochemistry, Faculty of Science, Alexandria University, Egypt, Abstract, V. 2, p. 144.
- Mohammed, F.H., Moghazi, A.M., Hassanen, M.A., 2000. Geochemistry, petrogenesis and tectonic setting of late Neoproterozoic Dokhan-type volcanic rocks in the Fatira area, Eastern Egypt. Internat. J. Earth Sci. 88, 764–777.
- Morimoto, N., Fabries, J., Ferguson, A., Ginzburg, I., Ross, M., Seifert, F., Zussman, J., Aoki, K., Gottardi, G., 1988. Nomenclature of pyroxenes. Mineralo. Magazine 52, 535–550.
- Moussa, E.H., 1998. Geochronological Studies of Some Granitoids; Application to Geochemical Evolution and Tectonic History of the Northern Eastern Desert, Egypt. Ph. D. Thesis. Ain Shams University, Egypt, p. 284.
 Moussa, E.M.M., Stern, R.J., Manton, W.I., Ali, K.A., 2008. SHRIMP zircon dating and Sm/Nd
- Moussa, E.M.M., Stern, R.J., Manton, W.I., Ali, K.A., 2008. SHRIMP zircon dating and Sm/Nd isotopic investigations of Neoproterozoic granitoids, Eastern Desert, Egypt. Precambrian Res. 160, 341–356.
- Moyen, J.F., Martin, H., 2012. Forty years of TTG research. Lithos 148, 312-336.
- Obeid, M.A., Azer, M.K., 2015. Pan-African adaktitic rocks of the north Arabian-Nubian Shield: petrological and geochemical constraints on the evolution of the Dokhan volcanics in the north Eastern Desert of Egypt. Int. J. Earth Sci. 104, 541–563.
- Pearce, J.A., 1983. Role of the sub-continental lithosphere in magma genesis at active continental margins. In: Hawkesworth, C.J., Norry, M.J. (Eds.), Continental Basalts and Mantle Xenoliths. Shiva, Nantwich, pp. 230–249.
- Pearce, J.A., 1996. Sources and settings of granitic rocks. Episodes 19, 120-125.
- Pearce, J.A., Gale, G.P., 1977. Identification of ore deposition environment from trace elements geochemistry of associated igneous host rocks. Volcanic Processes in Ore Genesis. Inst. Geological Society of London, Special Publication 7, pp. 14–24.
- Pearce, J.A., Harris, N.B.W., Tindle, A.G., 1984. Trace element discrimination diagrams for the tectonic interpretation of granitic rocks. J. Petrol. 25, 956–983.
- Ressetar, R., Monard, J.R., 1983. Chemical composition and tectonic setting of the Dokhan Volcanic formation, Eastern Desert, Egypt. J. Afr. Earth Sci. 1, 103–112.
- Richards, J., Kerrich, R., 2007. Adakite-like rocks: their diverse origins and questionable role in metallogenesis. Econ. Geol. 102 (4), 537–576.
- Rickwood, P.C., 1989. Boundary lines within petrologic diagrams, which use oxides of major and minor elements. Lithos 22, 247–263.
- Ridolfi, F., Renzulli, A., Puerini, M., 2010. Stability and chemical equilibrium of amphibole in calc-alkaline magmas: an overview, new thermobarometric formulations and application to subduction-related volcanoes. Contrib. Mineral. Petrol. 160, 45–66.
- Roeder, P.L., Emslie, R.F., 1970. Olivine-liquid equilibrium. Contrib. Mineral. Petrol. 29, 275–289.
- Samuel, M.D., Be'eri-Shlevin, Y., Azer, M.K., Whitehouse, M.J., Moussa, H.E., 2011. Provenance of conglomerate clasts from the volcano-sedimentary sequence at Wadi Rutig in southern Sinai, Egypt as revealed by SIMS U-Pb dating of zircon. Gondwana Res. 20, 450–464.
- Stacey, J.S., Stoeser, D.B., Greenwood, W.R., Fischer, L.B., 1984. U-Pb zircon geochronology and geological evolution of the Halaban-Al Amar region of the Eastern Arabian Shield, Kingdom of Saudi Arabia. J. Geol. Soc. Lond. 141, 1043–1055.
- Stern, R.J., 1994. Arc assembly and continental collision in the Neoproterozoic East African Orogen: implications for the consolidation of Gondwanaland. Ann. Rev. Earth Planet. Sci. 22 (1), 319–351.
- Stern, R.J., Gottfried, D., 1986. Petrogenesis of a late Precambrian (575–600 Ma) bimodal suite in northeast Africa. Contrib. Mineral. Petrol. 92 (4), 492–501.
- Stern, R.J., Johnson, P., 2010. Continental lithosphere of the Arabian Plate: a geologic, petrologic, and geophysical synthesis. Earth-Sci. Rev. 101 (1–2), 29–67.
- Stern, C.R., Kilian, R., 1996. Role of the subducted slab, mantle wedge and continental crust in the generation of adakites from the Andean Austral volcanic zone. Contrib. Mineral. Petrol. 123, 263–281.
- Stern, R.J., Gottfried, D., Hedge, C.E., 1984. Late Precambrian rifting and crustal evolution in the Northeastern Desert of Egypt. Geology 12 (3), 168–172.
- Stern, R.J., Ali, K.A., Liégeois, J.P., Johnson, P.R., Kozdroj, W., Kattan, F.H., 2010. Distribution and significance of pre-Neoproterozoic zircons in juvenile Neoproterozoic igneous rocks of the Arabian-Nubian Shield. Am. J. Sci. 310 (9), 791–811.
- Sun, S.S., McDonough, W.F., 1989. Chemical and isotopic systematics of oceanic basalts: Implications for mantle composition and processes. In: Saunders, A.D., Norry, M. (Eds.), Magmatism in Ocean Basins. Geological Society of London Special Publication 42, pp. 313–345.
- Sylvester, P.J., 1989. Post-collisional alkaline granites. Journal of Geology 97, 261–280.
 Whalen, J.B., Currie, K.L., Chappell, B.W., 1987. A-type granites: geochemical characteristics, discrimination and petrogenesis. Contrib. Mineral. Petrol. 95 (4), 407–419.
- Wilde, S.A., Youssef, K., 2000. Significance of SHRIMP U-Pb dating of the imperial porphyry and associated Dokhan Volcanics, Gebel Dokhan, north Eastern Desert, Egypt. J. Afr. Earth Sci. 31 (2), 403–413.
- Wilde, S., Youssef, K., 2002. A re-evaluation of the origin and setting of the Late Precambrian Hammamat Group based on SHRIMP U-Pb dating of detrital zircons from Gebel Umm Tawat, North Eastern Desert, Egypt. J. Geol. Soc. 159 (5), 595–604.
- Winchester, J.A., Floyd, P.A., 1977. Geochemical discrimination of different magma series and their differentiation products using immobile elements. Chem. Geol. 20, 325–343.
- Zhu, D.C., Zhao, Z.D., Pan, G.T., Lee, H.Y., Kang, Z.Q., Liao, Z.L., Wang, L.Q., Li, G.M., Dong, G.C., Liu, B., 2009. Early cretaceous subduction-related adakite-like rocks of the Gangdese Belt, southern Tibet: products of slab melting and subsequent melt-peridotite interaction? J. Asian Earth Sci. 34, 298–309.